Materials Science & Engineering A 907 (2024) 146690

Contents lists available at ScienceDirect

Materials Science & Engineering A

journal homepage: www.elsevier.com/locate/msea

Creep anisotropy of additively manufactured Inconel-738LC: Combined experiments and microstructure-based modeling

K. Kianinejad [a,*], R. Darvishi Kamachali [a], A. Khedkar [a], A.M. Manzoni [a], L. Agudo Jácome [a], S. Schriever [a], R. Saliwan Neumann [a], S. Megahed [b], C. Heinze [c], S. Kamrani [d], B. Fedelich [a]

[a] Federal Institute for Materials Research and Testing (BAM), Unter den Eichen 87, 12205 Berlin, Germany
[b] Technical University of Darmstadt, Center for Structural Materials, Grafenstraße 2, 64283 Darmstadt, Germany
[c] Siemens Energy, SE GS D AM TEC MA, Huttenstr. 12, 10553 Berlin, Germany
[d] Technical University of Berlin, Institute of Material Science and Technology, Straße des 17. Juni 135, 10623 Berlin, Germany

ARTICLE INFO

Keywords:
Additive manufactured Ni-base superalloys
Creep anisotropy
Crystal plasticity
Superlattice extrinsic stacking faults

ABSTRACT

The current lack of quantitative knowledge on processing-microstructure–property relationships is one of the major bottlenecks in today's rapidly expanding field of additive manufacturing. This is centrally rooted in the nature of the processing, leading to complex microstructural features. Experimentally-guided modeling can offer reliable solutions for the safe application of additively manufactured materials. In this work, we combine a set of systematic experiments and modeling to address creep anisotropy and its correlation with microstructural characteristics in laser-based powder bed fusion (PBF-LB/M) additively manufactured Inconel-738LC (IN738LC). Three sample orientations (with the tensile axis parallel, perpendicular, and 45° tilted, relative to the building direction) are crept at 850 °C, accompanied by electron backscatter secondary diffraction (EBSD), scanning electron microscopy (SEM) and transmission electron microscopy (TEM) investigations. A crystal plasticity (CP) model for Ni-base superalloys, capable of modeling different types of slip systems, is developed and combined with various polycrystalline representative volume elements (RVEs) built on the experimental measurements. Besides our experiments, we verify our modeling framework on electron beam powder bed fusion (PBF-EB/M) additively manufactured Inconel-738LC. The results of our simulations show that while the crystallographic texture alone cannot explain the observed creep anisotropy, the superlattice extrinsic stacking faults (SESF) and related microtwinning slip systems play major roles as active deformation mechanisms. We confirm this using TEM investigations, revealing evidence of SESFs in crept specimens. We also show that the elongated grain morphology can result in higher creep rates, especially in the specimens with a tilted tensile axis.

1. Introduction

Additive Manufacturing (AM) is rapidly progressing towards solidifying its position as a prominent processing technique. This stems, among several advantages, from the potential of this technique for automation [1], precise prototyping [2] and repair applications [3]. Safe and comprehensive application of the AM, however, is still a technological challenge. Among several aspects, the nonequilibrium microstructures emerging during the AM process remains elusive so far: The thermo-chemo-structural couplings between directional temperature gradients and evolving microstructures result in diverse, hierarchical textures, phases, and defects' distributions. These, in turn, impact the ultimate properties of AMed materials, which are then expected to compete with conventionally produced materials.

The interest in AMed Ni-base superalloys and their potential applications has recently been growing [4,5]. The creep performance, resulting from the γ/γ' microstructure, is of technological significance for these alloys. While revealing similar γ/γ' phases, the AMed Ni-base superalloys are found to exhibit columnar grains with <001> texture, typically aligned parallel to the build direction with strong compositional inhomogeneity within the microstructure. These process-specific features differ significantly from conventionally manufactured microstructures [6,7] and result in an anisotropic response in both secondary and tertiary creep, even after heat treatment [8–10].

A substantial amount of research has been devoted (i) to identifying and minimizing microstructure defects during AM process [11–13], (ii) to investigate the influence of the processing parameters on the microstructure [14–16] and, (iii) to characterize the correlation between

* Corresponding author.
E-mail addresses: kaveh.kianinejad@bam.de (K. Kianinejad), bernard.fedelich@bam.de (B. Fedelich).

https://doi.org/10.1016/j.msea.2024.146690
Received 22 December 2023; Received in revised form 14 May 2024; Accepted 20 May 2024
Available online 22 May 2024

the AMed microstructure and mechanical properties [17–19]. Yet, due to the large space of processing parameters, experimental characterization of the processing-microstructure–property relationships remains challenging. This currently limits the safe adoption of AM process for Ni-base superalloys. In this context, material modeling is a promising, powerful means, as demonstrated in recent studies [20–22], to explore the correlation between the microstructural and mechanical properties of AMed materials.

A broad range of creep deformation mechanisms has been revealed in conventionally manufactured Ni-base superalloys, including dislocation motion (glide and climb), shearing of the precipitates by matrix dislocations, leaving antiphase boundaries (APB) or forming superlattice intrinsic or extrinsic stacking faults (SISF/SESF) or microtwinning, as well as grain boundary sliding and diffusion (see, e.g., [23,24]). These led to the development of deformation maps, describing dominant deformation mechanisms as a function of the temperature and the stress during creep [25,26]. A comprehensive overview of the modeling techniques applied to Ni-base superalloys at different scales can be found in [24]. Yet, extending and applying this knowledge to AMed Ni-base superalloys requires careful consideration of their special microstructure.

Crystal plasticity finite element methods (CPFEM), combining crystal plasticity (CP) constitutive models with an idealized description of microstructural features, is a powerful tool that allows an explicit coupling of the microstructure and the mechanical behavior [27–30]. Several CP models have been proposed for studying creep in single crystal Ni-base superalloys, which either phenomenologically or mechanistically incorporate the experimentally observed creep deformation mechanisms at different temperatures and stresses. Here, the low-temperature regime for which the γ' microstructure remains stable and the high-temperature regime for which precipitate coarsening and rafting occur should be distinguished. The CPFEM was also recently applied to study the creep anisotropy of AMed IN738LC. Prasad et al. [31] implemented a CPFEM approach based on the CP model presented in [32] and on the texture characteristics for predicting creep anisotropy in AMed IN738LC at 980 °C with a Voxel model of the grain structure. Fernandez-Zelaia et al. [33] also utilized the CPFEM with a Voxel model of the grain structure and the measured crystallographic texture to predict the creep anisotropy of electron beam powder bed fusion (PBF-EB/M) manufactured IN738LC at 850 °C. It was demonstrated that the approach can capture partially stationary creep anisotropy. The underlying CP here did not account for $< \bar{1}12 > \{111\}$ slip systems. Instead, the octahedral glide was assumed to be controlled by a non-Schmid yield stress inspired by an estimate of the strengthening effect due to Kear-Wilsdorf locks (see, e.g., [23]).

In the low-temperature regime ($T \leq 850$ °C), the dominant contribution to creep strains is found to be due to macroscopic glide along $a < \bar{1}12 > \{111\}$ slip systems [23,24,34–39], which at the microscopic level can be explained by the formation of superlattice intrinsic or extrinsic stacking faults, microtwins or stacking faults ribbons. To date, the models devoted to the low-temperature regime usually include $< 112 > \{111\}$ type slip systems, in addition to the octahedral and (possibly) cubic slip systems. On the other hand, the majority of the models consider either only SISF based mechanisms [40], or SESF based mechanisms such as micro-twinning [41], or make no formal distinction between the two glide directions [37,42,43]. However, the glide of superpartial dislocations in the $< 11\bar{2} >$ and in the $< \bar{1}12 >$ direction leave behind in the γ' phase either SISFs or SESFs, which are complex stacking faults of different crystallographic nature and energy. Thus, the $< 11\bar{2} > \{111\}$ and the $< \bar{1}12 > \{111\}$ slip systems must be treated as different systems, a distinction that was so far missing in the investigations. These aspects are brought to light in the current study.

In this work, we combined experimental investigations and CP modeling to systematically study the creep anisotropy of AMed IN738LC at 850 °C as a pertinent temperature for industrial application (see, e.g., [44,45]). At this temperature, the γ' microstructure can be regarded as relatively stable up to about 1000 h [46,47]. We performed creep tests on laser-based powder bed fusion (PBF-LB/M) manufactured material in three different specimen orientations. Electron backscatter diffraction (EBSD) and transmission electron microscopy (TEM) were used to investigate the microstructure of AMed samples. We developed a microstructure-based CPFEM modeling framework to investigate the influence of the deformation mechanisms, crystallographic texture, and grain morphology on creep anisotropy. The essential modeling constituents required for describing the stationary creep anisotropic response were identified and discussed. The influence of the deformation mechanisms on the creep response of polycrystalline IN738LC was modeled and investigated for the first time. We showed that the current model can capture the essential trends of the anisotropic stationary creep response of PBF-EB/M and PBF-LB/M manufactured IN738LC at 850 °C. Thereby, the focus rather lies on the identification of the main factors influencing creep anisotropy than a comprehensive modeling of the whole creep response. Additionally, we demonstrated that our approach can sufficiently link the microstructure and creep anisotropy and requires only the creep response in one specimen orientation for the model calibration.

2. Experimental and modeling methods

2.1. Creep tests and characterizations

We performed two sets of creep tests at 850 °C on PBF-LB/M manufactured IN738LC samples. Table S1 in the Supplementary Material (SM) gives the alloy powder composition. All specimens were fabricated with identical process parameters but different dimensions and orientations concerning the AM build direction (BD). The PBF-LB/M was performed on an EOS-M290 machine with a volume energy density of 69 J/mm^3 and a layer thickness of 40 μm. The exact process parameters cannot be published but are based on the following main parameters, which can be found in the literature (e.g. [48]): (1) Laser power of 225 W, (2) Scan speed of 1010 m/s, and (3) Hatch distance of 80 μm. The meander scanning strategy was applied in an alternating laser scanning pattern with 67° rotation after each layer. The samples were subsequently processed by hot isostatic pressing (HIP) and solution heat treatment (1120 °C/2 h / air cooling) followed by 24 h aging at 840 °C and subsequent air cooling. During the heat treatment, an argon atmosphere was applied to avoid oxidation. Both as-built and heat-treated specimens were microcrack-free. An average relative density of 99.98% was identified for the heat-treated, HIPed, and undeformed specimens. The details of relative density measurements, light microscopy micrographs, and SEM images of the same specimens can be found [49].

To investigate the creep anisotropy, we performed creep tests in three specimen orientations: (1) Vertical Direction (VD) with the tensile axis aligned with the BD, (2) Horizontal Direction (HD) with the tensile axis perpendicular to the BD, and (3) Diagonal Direction (DD) where the tensile axis lies in VD-HD-plan with a $\theta = 45°$ angle to the BD (see Fig. 1). The creep tests were performed at constant force according to the standard DIN EN ISO 204:2019-04 [50]. The temperature was measured with three thermocouples of type S tied along the gauge length, and the specimen elongation was measured using ceramic axial extensometers.

In addition to our experiments, a creep data set from [33], fabricated by PBF-EB/M technique utilizing a contour melt scanning pattern, was adopted for additional validation of our modeling approach. The testing method and critical process parameter details can be found in [51]. These creep tests are on three specimen orientations, HD, VD, and DD, with a tilt angle of $\theta = 54.7°$. We refer to these as 'PBF-EB/M' manufactured specimens and to our own experiments as 'PBF-LB/M' specimens. Table 1 summarizes our creep tests and related specimen parameters.

The EBSD analysis was used to characterize the grain morphology and crystallographic texture and to obtain related inverse pole figures

Table 1
Summary of creep tests. All tests were performed at 850 °C. *Creep data set 3 is adopted from [33,51], referred to as PBF-EB/M specimens.

Creep tests	Stress level [MPa]	Manufacturing method	Specimen orientation	Gauge length [mm]	Gauge diameter [mm]
Set 1	220, 360	PBF-LB/M	HD	25.0	6.00
Set 2	200, 240	PBF-LB/M	HD, VD, DD	24.5	5.00
Set 3*	175, 210, 240, 275	PBF-EB/M	VD, DD, HD	25.4	6.35

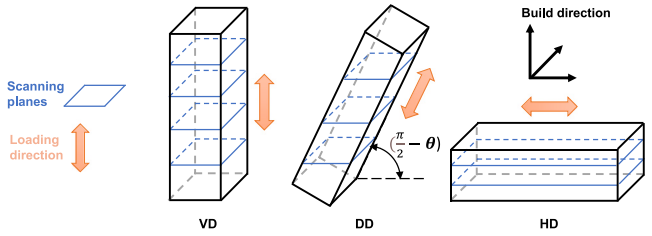

Fig. 1. Specimens' orientations with respect to the loading direction in our creep tests. Scanning planes are shown accordingly.

(IPF). Crept specimens were cut along and perpendicular to the tensile axis and prepared by mechanical grinding. The imaging was carried out using a LEO Gemini 1530 VP (Zeiss) SEM with 70° tilted specimens operating at 20 kV and equipped with eFlash HD Detector. To ensure statistical representativity, a total area of 126 mm^2 (eight images) was measured with a step size of 5.76 μm. The MTEX software was then used to combine and evaluate the data [52]. Grain size and aspect ratio were determined by fitting ellipses to the detected grains using the built-in MTEX algorithms. The length of the ellipse short axis is defined as the grain size (equivalent diameter) and the ratio of the long axis to the short axis is defined as the grain aspect ratio. The EBSD data were smoothed and de-noised before grain detection. A minimum misorientation angle of 10° and a minimum equivalent grain diameter of 50 μm were used as grain detection criteria. We performed TEM measurements on a JEOL JEM-2200FS Field Emission TEM (JEOL Ltd., Tokyo, Japan) operating at 200 kV, using bright-field (BF) and dark-field (DF) conventional (C) TEM imaging. TEM specimens were cut from the gauge length of a crept specimen (240 MPa and creep rupture strain of 2%) perpendicular to the tensile axis with a thickness of 0.5 mm. The cut specimens were polished to P1200 grit, then 3 mm sized disks were punched from the 120 um thick slices. The disks were electropolished with a solution of 83 vol. % ethanol, 7 vol. % glycerin, and 10 vol. % perchloric acid at −7 °C using a voltage of 30 V. Additionally, we carried out a microstructural investigation using optical microscopy (LM, Leica Microsystems), scanning electron microscopy (SEM, CamScan Series 2, Obducat, Sweden), and energy dispersive spectroscopy (EDS) measurements. Size distribution and volume fraction of primary and secondary γ' precipitates were analyzed using the MIPAR image analysis software [53].

2.2. CPFEM modeling approach

CPFEM-based RVEs applied to polycrystalline materials enable direct consideration of microstructural features. Microstructure-based modeling of Ni-base superalloys has been increasingly addressed [54–56], with recent AM-specific RVE models incorporating crystallographic orientation and grain morphology [31,33,57]. In the current study, we developed a comprehensive CPFEM approach capable of correlating AM-specific microstructure properties with creep behavior, consisting of the deformation mechanism-based crystal plasticity model and representative volume element (RVE) models with different levels of microstructural complexity. The current framework then enables a systematic investigation of contributing factors to creep anisotropy in AMed IN738LC presented here for the first time.

The two-phase microstructure of these alloys, consisting of the FCC Ni-rich matrix with solute elements (such as Cr and Co) and the $L1_2$ Ni_3Al ordered precipitates, also maintains a variety of linear and planar defects, which in turn leads to a range of various deformation mechanisms. Figure S1 in the Supplementary Material (SM) shows an overview of the possible slip systems in a {111} plane of the $L1_2$ structure. The main deformation mechanisms that have been frequently discussed in the context of low-temperature creep include:

1. The glide of $a/2 < 110 >$ dislocations through the matrix channels that deposit segments on the γ/γ' interfaces behind them. These segments reduce the local stresses in the channels, leading to kinematic hardening.
2. The shearing of the γ' precipitates by $a/2 < 110 >$ dislocation pairs coupled by Anti-Phase Boundary (APB) (see, e.g., [58]), which also contribute to deformation by the slip systems from the type $\{111\} < 110 >$.
3. The formation and propagation of defects, including microtwins resulting from the initial formation of SESFs, and driven by the diffusion-assisted glide of $a/6 < \bar{2}11 >$ partial dislocation pairs in the γ' phase [26,36,39,59,60]. Isolated SESFs and microtwins macroscopically amount to the activation of slip systems from the type $\{111\} < \bar{2}11 >$ [34,35,37].
4. The formation and propagation of planar defects driven by $a/3 < 2\bar{1}\bar{1} >$ superpartials like SF-ribbons resulting from the nucleation of SISF at the γ/γ' interfaces (see, e.g., [38,60–62]). Macroscopically, isolated SISFs and SF-ribbons amount to the operation of slip systems from the type $\{111\} < 2\bar{1}\bar{1} >$ [35,42].
5. Macroscopic evidence suggests the existence of cubic slip in $< 111 >$ oriented crystals under tension (see, e.g., [63,64]). However, its physical origin remained controversial for decades. Discrete dynamic dislocation simulations [65] showed that for the combinations of slip systems activated in $< 111 >$ tension specimens, the Burgers vectors of the interface dislocations compensate. In turn, the hardening observed in other orientations disappears, leading to a localization of the deformation on macroscopic {001} planes.
6. The thermally activated local or general climb process in which dislocation segments climb around the γ' precipitates [66,67].

It should be mentioned that, in reality, no sharp limits can be given for the temperature and stress ranges in which a particular mechanism becomes active or inactive. Instead, it is rather likely that multiple deformation mechanisms are operative at the same time, but one or several mechanisms are dominant within a temperature and loading range. Since the present study focuses on creep at 850 °C, it has been assumed that rafting can be neglected. The cubic slip effect is accounted for by an appropriate description of hardening, as shown below. In turn, three families of slip systems are considered, which are related to the mechanisms above:

- Octahedral systems (1, 2 and 6): {111} <110>
- SESF-related systems (3): $\{111\} < \bar{2}11>$
- SISF-related systems (4): $\{111\} <2\bar{1}\bar{1} >$

The consideration of SISF- and SESF-related systems for 850 °C is based on the fact that recent studies reported experimental evidence for the existence of related deformation mechanisms such as microtwinning and SF-ribbons in a temperature range of 700 to 950 °C [26,60].

Furthermore, it is pointed out that climbing around the particles leads at the macroscopic scale to the same deformation as octahedral glide because there is no preferred climb direction for a dislocation initially gliding on a random octahedral plane between cubic or spherical precipitates. The reader is referred to [67] among others for a detailed study of the climbing process in Ni-base superalloys with cubic precipitates.

2.2.1. Crystal plasticity model

We included the five previously mentioned deformation mechanisms. For the macroscopic stress $\boldsymbol{\sigma}$, we consider the volume average of the stresses in both phases

$$\boldsymbol{\sigma} = (1-f)\boldsymbol{\sigma}_{\gamma} + f\boldsymbol{\sigma}_{\gamma'}, \tag{1}$$

where f denotes the volume fraction of the γ' precipitates. The stresses in each phase can be readily estimated with the (oversimplified) approximation of a homogeneous strain $\boldsymbol{\varepsilon} = \boldsymbol{\varepsilon}_{\gamma} = \boldsymbol{\varepsilon}_{\gamma'}$:

$$\boldsymbol{\sigma}_{\gamma} = \boldsymbol{\sigma} + f \overset{<4>}{\mathbf{C}} : \left(\boldsymbol{\varepsilon}^{in}_{\gamma'} - \boldsymbol{\varepsilon}^{in}_{\gamma}\right), \tag{2}$$

$$\boldsymbol{\sigma}_{\gamma'} = \boldsymbol{\sigma} + (1-f) \overset{<4>}{\mathbf{C}} : (\boldsymbol{\varepsilon}^{in}_{\gamma} - \boldsymbol{\varepsilon}^{in}_{\gamma'}), \tag{3}$$

where $(\boldsymbol{\varepsilon}^{in}_{\gamma} - \boldsymbol{\varepsilon}^{in}_{\gamma'})$ is the difference of the inelastic strains between both phases and $\overset{<4>}{\mathbf{C}}$ denotes the elastic stiffness tensor, assumed to be identical in both phases. The deformation typically starts in the γ matrix and Eq. (2) naturally implies kinematic hardening that reaches saturation when the precipitates are sheared by dislocations. Eqs. (2) and (3) are too stiff, yielding high internal stresses in both phases. Less stiff estimates can be obtained using Eshelby's inclusion theory (see, e.g., [68]), which still is not appropriate for cuboidal γ' precipitates with high volume fractions. A more general but phenomenological approach is to replace $\overset{<4>}{\mathbf{C}}$ by a fourth-order tensor $\overset{<4>}{\boldsymbol{\Omega}}$ of cubic symmetry:

$$\boldsymbol{\sigma}_{\gamma} = \boldsymbol{\sigma} + f \overset{<4>}{\boldsymbol{\Omega}} : \left(\boldsymbol{\varepsilon}^{in}_{\gamma'} - \boldsymbol{\varepsilon}^{in}_{\gamma}\right), \tag{4}$$

$$\boldsymbol{\sigma}_{\gamma'} = \boldsymbol{\sigma} + (1-f) \overset{<4>}{\boldsymbol{\Omega}} : (\boldsymbol{\varepsilon}^{in}_{\gamma} - \boldsymbol{\varepsilon}^{in}_{\gamma'}). \tag{5}$$

We found that a proper choice for this tensor suppresses hardening in $< 111 >$ oriented uni-axial specimens when only octahedral slip systems are operating, hence accounting for the so-called cubic slip effect without resorting to cubic slip systems [69]. For this purpose, $\overset{<4>}{\boldsymbol{\Omega}}$ is decomposed into the three orthogonal basis tensors, the so-called Kelvin modes [70]:

$$\overset{<4>}{\boldsymbol{\Omega}} = \alpha \overset{<4>}{\mathbf{J}} + \beta \overset{<4>}{\mathbf{L}} + \delta \overset{<4>}{\mathbf{M}}. \tag{6}$$

The basis tensors are defined with the base $\mathbf{e}_i$ in the crystal axes as

$$\overset{<4>}{\mathbf{J}} := \frac{1}{3}\delta_{ij}\delta_{kl}\mathbf{e}_i \otimes \mathbf{e}_j \otimes \mathbf{e}_k \otimes \mathbf{e}_l$$

$$\overset{<4>}{\mathbf{L}} := \overset{<4>}{\mathbf{I}} - \overset{<4>}{\mathbf{S}}$$

$$\overset{<4>}{\mathbf{M}} := \overset{<4>}{\mathbf{S}} - \overset{<4>}{\mathbf{J}},$$

with the identity tensor

$$\overset{<4>}{\mathbf{I}} := \delta_{ik}\delta_{jl}\mathbf{e}_i \otimes \mathbf{e}_j \otimes \mathbf{e}_k \otimes \mathbf{e}_l,$$

and

$$\overset{<4>}{\mathbf{S}} := \sum_{i=1}^{3} \mathbf{e}_i \otimes \mathbf{e}_i \otimes \mathbf{e}_i \otimes \mathbf{e}_i.$$

The product of $\overset{<4>}{\mathbf{J}}$ with any deviatoric tensor vanishes, in particular, $\overset{<4>}{\mathbf{J}} : \left(\boldsymbol{\varepsilon}^{in}_{\gamma'} - \boldsymbol{\varepsilon}^{in}_{\gamma}\right) = \mathbf{0}$. Hence the representation (6) can be reduced to

$$\overset{<4>}{\boldsymbol{\Omega}} = \beta \overset{<4>}{\mathbf{L}} + \delta \overset{<4>}{\mathbf{M}} \tag{7}$$

without loss of generality. It can be shown that kinematic hardening in uniaxially loaded $< 111 >$ crystals exactly vanishes when $\beta = 0$, while the magnitude of kinematic hardening in the $< 001 >$ direction is controlled by δ, which is taken as an adjustable parameter.

The total inelastic strain rate $\dot{\boldsymbol{\varepsilon}}^{in}$ is composed of the contribution of all slip systems:

$$\dot{\boldsymbol{\varepsilon}}^{in} = \dot{\boldsymbol{\varepsilon}}^{in}_{oct} + \dot{\boldsymbol{\varepsilon}}^{in}_{SISF} + \dot{\boldsymbol{\varepsilon}}^{in}_{SESF} \tag{8}$$

where $\dot{\boldsymbol{\varepsilon}}^{in}_{oct}$ is the inelastic strain rate due to the octahedral slip systems, $\dot{\boldsymbol{\varepsilon}}^{in}_{SISF}$ the inelastic strain rate due to the SISF-related systems and $\dot{\boldsymbol{\varepsilon}}^{in}_{SESF}$ the inelastic strain rate due to the SESF-related systems. To simplify, it is assumed that microtwins and SF-ribbons control the creep rates within the two last families of slip systems. Since microtwins and SF-ribbons can shear both matrix and precipitates, the corresponding strain rates apply for both matrix and precipitates in contrast to $\dot{\boldsymbol{\varepsilon}}^{in}_{oct}$ that must be split in the contribution of both phases:

$$\dot{\boldsymbol{\varepsilon}}^{in}_{oct} = (1-f)\dot{\boldsymbol{\varepsilon}}^{in}_{oct,\gamma} + f\dot{\boldsymbol{\varepsilon}}^{in}_{oct,\gamma'}. \tag{9}$$

For each slip system family χ, where χ corresponds to either SISF, SESF, (oct, γ) or (oct, γ'), the corresponding inelastic strain rate, $\dot{\boldsymbol{\varepsilon}}^{in}_{\chi}$, can then be formulated as the sum of the contributions of all systems of the family:

$$\dot{\boldsymbol{\varepsilon}}^{in}_{\chi} = \frac{1}{2}\sum_{g=1}^{N_{\chi}} \left[\left(\mathbf{m}_{\chi,g} \otimes \mathbf{n}_{\chi,g}\right) + \left(\mathbf{n}_{\chi,g} \otimes \mathbf{m}_{\chi,g}\right)\right] \dot{\gamma}^{in}_{\chi,g} \tag{10}$$

For a slip system g, the unit vector $\mathbf{m}_{\chi,g}$ corresponds to the slip direction, and $\mathbf{n}_{\chi,g}$ refers to normal to the slip plane. The number of slip systems, N_{χ}, is 24 in the case of the octahedral slip systems and 12 in other cases. Table 2 summarizes all slip system families' slip planes and directions. Note that glide is equally possible in both directions in the case of the octahedral slip systems, which does not apply to the SISF-related and SESF-related systems.

The dependence of the shear rates $\dot{\gamma}^{in}_{\chi,g}$ on the Resolved Shear Stresses (RSS) is assumed to follow a thermally activated law (see, e.g., [71])

$$\dot{\gamma}^{in}_{\chi,g} = A_{\chi} \exp\left(-\frac{Q_{\chi}}{k\,T}\right) \sinh\left[\frac{V_{\chi}b^3}{k\,T}\tau_{\chi,c}\; H\left(y_{\chi,g}; s_{\chi}\right)\right], \tag{11}$$

with $y_{\chi,g} = \frac{\langle \tau_{\chi,g} \rangle}{\tau_{\chi,c}}$ and $H(y;s) = y\left[1-(1+y^s)^{(-\frac{1}{s})}\right]$. Here $\langle x \rangle$ denotes the MacCauley bracket, i.e., $\langle x \rangle = x$ if $x \geq 0$ and $\langle x \rangle = 0$ if $x < 0$. $\tau_{\chi,g}$ represents the relevant RSS for the considered mechanism, i.e., $\tau_{\chi,g} = \mathbf{m}_{\chi,g} \cdot \boldsymbol{\sigma} \cdot \mathbf{n}_{\chi,g}$ for the SISF or SESF-related systems and $\tau_{\chi,g} = \mathbf{m}_{\chi,g} \cdot \boldsymbol{\sigma}_{\gamma} \cdot \mathbf{n}_{\chi,g}$, respectively, $\tau_{\chi,g} = \mathbf{m}_{\chi,g} \cdot \boldsymbol{\sigma}_{\gamma'} \cdot \mathbf{n}_{\chi,g}$ for octahedral glide in the matrix or in the precipitates. $\tau_{\chi,c}$ denotes the critical stress for the corresponding deformation mechanism, so that flow starts when $y_{\chi,g}$ exceeds 1. The function $H(y;s)$ ensures a smooth transition at the onset of yielding (see [72]). With a sufficiently high value of s, Eqs (11) amounts to a sharp threshold and

$$\dot{\gamma}^{in}_{\chi,g} \approx A_{\chi} \exp\left(-\frac{Q_{\chi}}{k\,T}\right) \sinh\left[\frac{V_{\chi}b^3}{k\,T}\left\langle \tau_{\chi,g} - \tau_{\chi,c} \right\rangle\right]. \tag{12}$$

In Eq. (11), V_{χ} corresponds to a dimensionless activation volume, A_{χ} to a prefactor, Q_{χ} is an activation energy, and k the Boltzmann constant. The parameters A_{SISF}, A_{SESF}, and $A_{(oct,\gamma)}$ are taken for simplicity to be time independent. In contrast, $A_{(oct,\gamma')}$ increases proportionally with the dislocation density λ_g on the γ/γ' interfaces for each slip system as

$$A_{(oct,\gamma')} = A_{(oct,\gamma'),0}\frac{\lambda_g}{\sqrt{2c}}, \tag{13}$$

with c being the precipitate size and $A_{(oct,\gamma'),0}$ a fitting parameter. The densities λ_g are related to the jump of the inelastic deformations at the γ/γ' interface as (see, e.g., [73])

$$\lambda_g = \frac{1}{b}\,\mathbf{m}_g \cdot \left(\boldsymbol{\varepsilon}^{in}_{\gamma} - \boldsymbol{\varepsilon}^{in}_{\gamma'}\right) \cdot \mathbf{n}_g. \tag{14}$$

Table 2
Definition of the three slip systems.

Slip plane		$(\bar{1}\bar{1}\bar{1})$	$(\bar{1}\bar{1}1)$	$(\bar{1}1\bar{1})$	$(\bar{1}11)$	$(1\bar{1}\bar{1})$	$(1\bar{1}1)$	$(11\bar{1})$	(111)	$(\bar{1}11)$	$(11\bar{1})$	$(1\bar{1}\bar{1})$	$(11\bar{1})$
Slip direction	OCT	$[\bar{1}01]$	$[0\bar{1}1]$	$[\bar{1}10]$	$[\bar{1}01]$	$[011]$	$[110]$	$[0\bar{1}1]$	$[110]$	$[101]$	$[\bar{1}10]$	$[101]$	$[011]$
		$[10\bar{1}]$	$[01\bar{1}]$	$[1\bar{1}0]$	$[10\bar{1}]$	$[0\bar{1}\bar{1}]$	$[\bar{1}\bar{1}0]$	$[01\bar{1}]$	$[\bar{1}\bar{1}0]$	$[\bar{1}0\bar{1}]$	$[1\bar{1}0]$	$[\bar{1}0\bar{1}]$	$[0\bar{1}\bar{1}]$
	SISF	$[\bar{2}11]$	$[1\bar{2}1]$	$[11\bar{2}]$	$[\bar{1}2\bar{1}]$	$[\bar{1}12]$	$[21\bar{1}]$	$[12\bar{1}]$	$[\bar{2}1\bar{1}]$	$[1\bar{1}2]$	$[\bar{1}21]$	$[\bar{2}11]$	$[\bar{1}\bar{1}2]$
	SESF	$[2\bar{1}\bar{1}]$	$[\bar{1}2\bar{1}]$	$[\bar{1}\bar{1}2]$	$[121]$	$[1\bar{1}2]$	$[\bar{2}11]$	$[\bar{1}2\bar{1}]$	$[211]$	$[\bar{1}1\bar{2}]$	$[1\bar{2}1]$	$[\bar{2}1\bar{1}]$	$[112]$

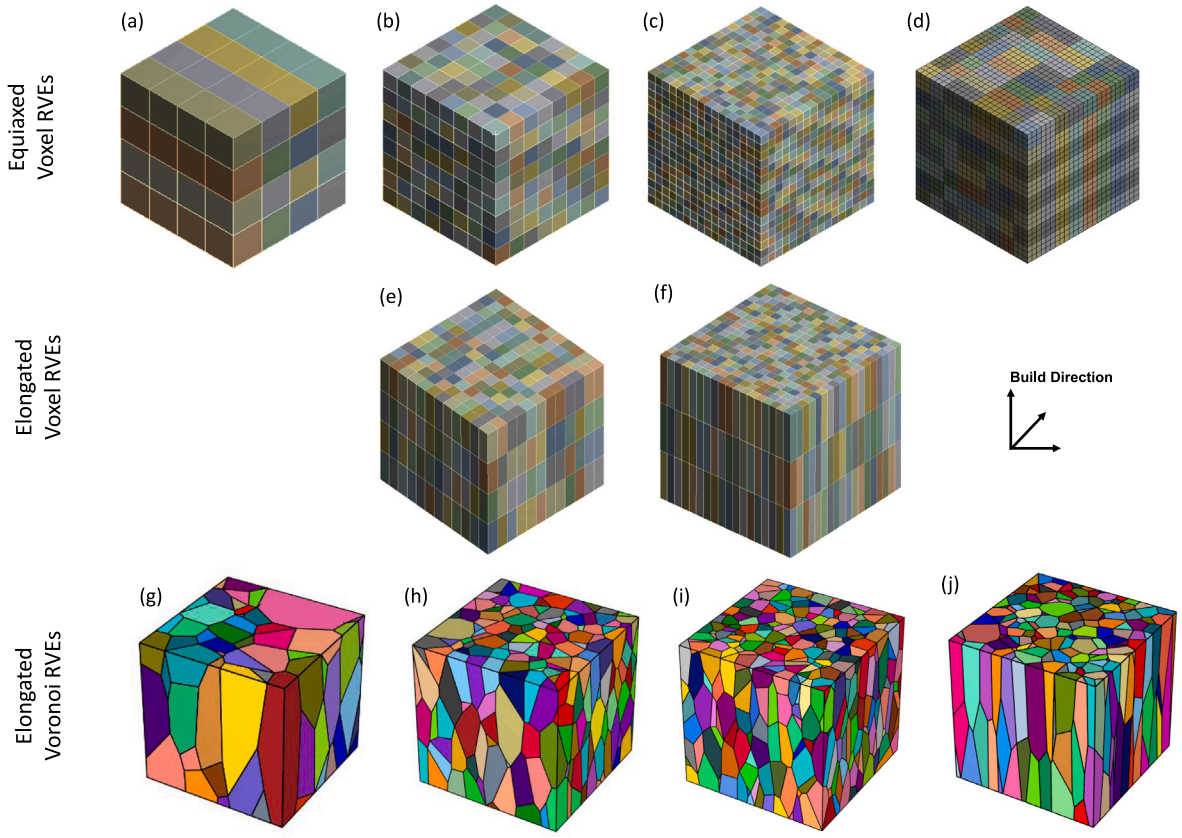

Fig. 2. Overview of the RVEs. RVEs (a), (c), (d), (e), (g), and (i) were used for model verification (see details in Appendix A, in the SM).

These two last relations translate the fact that precipitates shearing by $a/2 < 110 >$ dislocations consume the interface dislocations generated by octahedral matrix glide.

The relationship between the SF ribbons, the micro-twins, and the matrix dislocations is more intricate and has not been completely elucidated so far (see, e.g., the recent works [26,60–62,74]). Hence, since the SF ribbons and the micro-twins can move through both phases, it has been decided to uncouple these mechanisms as a first approximation for the sake of simplicity. In other words, their operation is assumed to not alter the interface dislocation densities λ_g.

2.2.2. Identification of the model parameters

For each slip system, $\chi = \{\text{SESF, SISF, } (oct,\gamma), (oct,\gamma')\}$, the parameters A_χ, V_χ and $\tau_{\chi,c}$ were fitted to the experimental results, except $\tau_{(oct,\gamma),c}$, which is equal to the Orowan stress τ_{Orowan}, i.e.,

$$\tau_{(oct,\gamma),c} = \tau_{Orowan} = \frac{C_{44}b}{\sqrt{3/2}w_{001}}, \tag{15}$$

with b the Burgers vector, $\sqrt{3/2}w_{001}$ the inter-precipitate channel width in a <111> plane, C_{44} the C_{1212} component of the stiffness tensor. The channel width in a <001> plane is denoted $w_{001} = \lambda - c$ with λ the periodicity length and c the cubic precipitate size. Any slip systems family χ can be simply deactivated by setting $A_\chi = 0$, while the remaining parameters of the system can be frozen to arbitrary values. This property will later be useful for independently assessing the capacity of each slip system family to capture the observed anisotropy. The model parameters were calibrated using the Z-Mat package from the software Z-Set [75], applying the Nelder–Mead or simplex optimization method [76] to minimize the objective function

$$F_e = \sum_{i=1}^{n} \frac{\int_0^{t_{end,i}} (\varepsilon_i^{exp}(t) - \varepsilon_i^{sim}(t))^2 dt}{\int_0^{t_{end,i}} (\varepsilon_i^{exp}(t))^2 dt}, \tag{16}$$

the sum of which is taken over the n creep tests with $t_{end,i}$ being the duration of the creep experiment i. The material parameters were calibrated using the results of our creep experiments for the stress levels 200 MPa, 220 MPa, 240 MPa, and 360 MPa. For the additional creep data from [33], the stress levels 175 MPa, 210 MPa, 240 MPa, and 275 MPa were used to calibrate the material parameters. In all cases, only the data from HD specimens were used, while the results of DD and VD specimens were used for validation and discussion.

The thermal activation energy Q_χ was arbitrarily set to zero since a single temperature (850 °C) was investigated. The parameters $\beta = 5.9 \times 10^{-3}$ and $\delta = 1.0$ that control the directionality of hardening via Eq. (7) were identified in previous work with test data from a single crystal superalloy with similar content of the γ' phase. The low value of 5.9×10^{-3} for β expresses the lack of hardening in the $< 111 >$ direction, while the value one for δ results from elastic stiffness after Eqs. (2) and

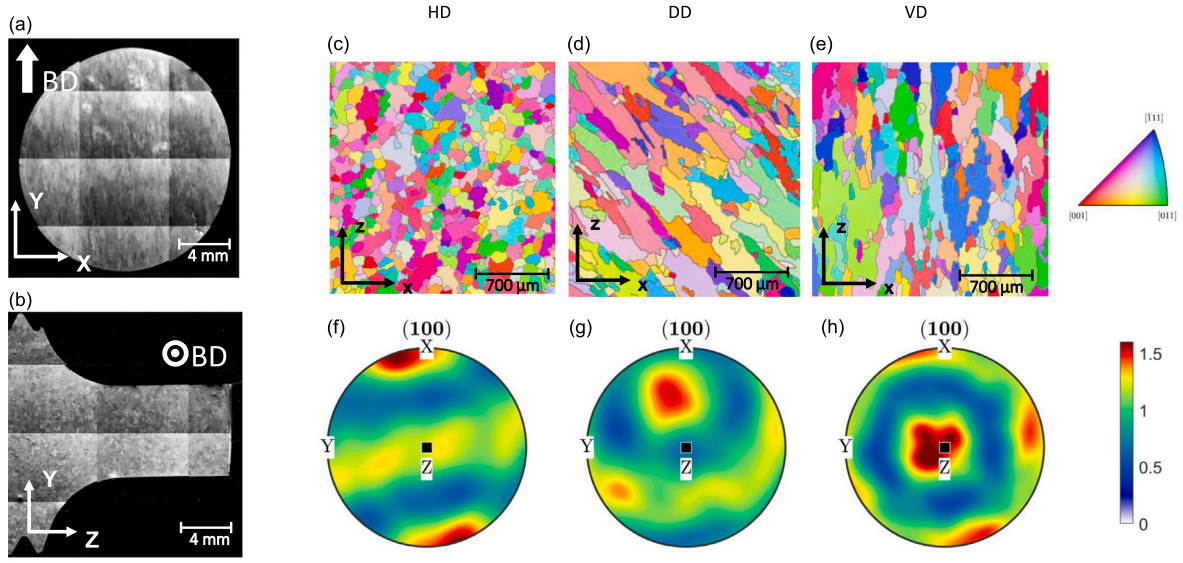

Fig. 3. Sample characterization: (a) and (b) light microscopy image of a measured area parallel and perpendicular to BD of AMed IN738LC, (c)–(e) examples of EBSD measurement for HD, DD, and VD, (f)–(g) ODF-pole figures of corresponding specimen orientations. The z-axis is the tensile axis.

(3). Also, a high value of the exponents $s = 9.0$ was found to yield a good agreement with single crystal data and approximately correspond to a behavior with a threshold as in Eq. (12). Other material parameters for IN738LC that were taken from the literature or directly measured are summarized in Table S2 in the SM.

2.2.3. Homogenization method

While a homogenization of the AMed manufactured microstructure is required, the refinement level of the mesoscale model required for capturing the anisotropy of the minimum creep rate is an unknown meta-parameter that shall be identified. In the present work, we utilized three types of RVEs with increasing levels of complexity addressing this issue: (1) Voxel RVEs with equiaxed grains and periodic boundary condition (PBC), (2) Voxel RVEs with elongated grains and PBC (3) Voronoi RVEs with elongated grains and uniform traction boundary condition (UTBC). The Voronoi RVEs were generated by the open-source software Neper [77]. All RVEs incorporate the discretized orientation distributions based on EBSD measurements for the respective specimen orientations. Type 2 and Type 3 RVEs account for the measured aspect ratio. Note that since the applied CP model is not size dependent, only the aspect ratio and variance of grain size distribution influence the model response. Regarding the impact of boundary conditions, the reader is referred to [78] for a systematic comparison of different BCs and their effect on RVE response. In general, it can be stated that UTBCs lead to a lower RVE effective stiffness (geometrically less constrained model) than PBCs and thus higher strain rates. However, with increasing size (here equivalent to the number of grains), the RVE responses with PBCs and UTBCs converge to the same limit [79].

Both RVE model types are converted to an Ansys [80] input file linked to a USERMAT user subroutine implementing the CP model described in the previous section. The Voxel RVEs are made of quadratic hexahedral elements with 20 integration points (Ansys, SOLID186 element type). The Voronoi RVEs consist of quadratic tetrahedral elements with 10 integration points (Ansys, SOLID187 element type). Fig. 2 gives an overview of the applied RVEs. Grain aspect ratios of 2.85 to 3 (based on our measurements) were chosen for RVE generation. The software MTEX was used for the identification of the orientation distribution and grain aspect ratio distribution [52]. For the data from [33], an aspect ratio of 6.0 (based on an estimation from their figures) was chosen. The details for the generation and verification of applied RVEs, as well as a study about the impact of the discretization, the number of grains, and the type of BC, are summarized in Appendix A in the SM.

3. Results

3.1. Microstructure characterization

The EBSD analyses reveal that our PBF-LB/M manufactured IN738LC alloy (AMed and subsequently annealed) develops an elongated grain structure with a relatively low texture index of 1.4 and {001} intensity peak in the BD. Fig. 3 shows the results. While the elongated grains are due to the strong temperature gradients, the low texture results from the alternating laser scanning pattern (67°), which assists with producing more homogeneous temperature fields and the subsequent heat treatment. The effect of laser scanning strategies and heat treatment on the AMed IN738LC's microstructure was previously studied [14,81] where a {001} -fiber texture and a cube texture were observed in the case of 67° rotating scanning pattern and 90° rotating scanning, respectively. The PBF-EB/M manufactured microstructure reported in [33] also exhibits a {001}-fiber texture in the BD. In contrast, our investigations reveal that the IN738LC microstructure consists of a combination of the two textures. Figs. 3f–h show the corresponding ODF-pole figures for VD, DD, and HD. All ODFs are calculated with the same half-width of 10° and are plotted in the same coordinate system to make the results comparable. The IN738LC microstructure with a low texture intensity is observable in all cases. For comparison, Figs. S3-d to S3-f show the pole figures of the ODF functions, reconstructed from [33], demonstrating a highly textured microstructure.

A minimum misorientation angle of 10° and a minimum equivalent grain radius of 25 µm were used as grain detection criteria. We separately calculated the grain size and aspect ratio distributions for both sections parallel to BD, with a total scanned area of 63 mm^2 and a total detected grain number of 4147 (Fig. S2-a), and perpendicular to BD, with a total scanned area of 63 mm^2 and a total detected grain number of 2409 (Fig. S2-b). We obtained the grain size on the parallel and perpendicular sections to be 100 and 105 µm, respectively, assuming a log-normal distribution. However, the grain aspect ratio distributions were found to be significantly different (2.85 and 1.5, respectively, on the parallel and perpendicular sections) due to the elongated grain structure parallel to BD. It should be noted that the grain size distribution is more sensitive to the choice of grain detection criteria than the grain aspect ratio.

SEM analyses on undeformed specimens reveal the existence of Ta-, Ti- and Nb-rich carbides mainly precipitated on the grain boundaries with a significant population, Fig. 4a–c. Some carbides were also

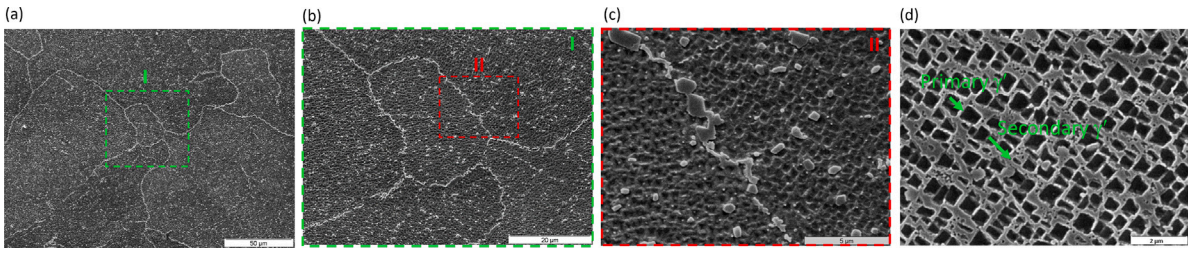

Fig. 4. SEM Analysis of AMed IN738LC after HIP and heat treatments: (a)–(c) show grain structure and precipitation of Ta-, Ti- and Nb-rich MC carbides with spherical-blocky morphology segregated mainly at the grain boundaries and low-temperature Cr-, Ta- and Nb-rich rod-shaped M23C6 carbides within the grains. (d) shows the formation of primary and secondary γ' precipitates.

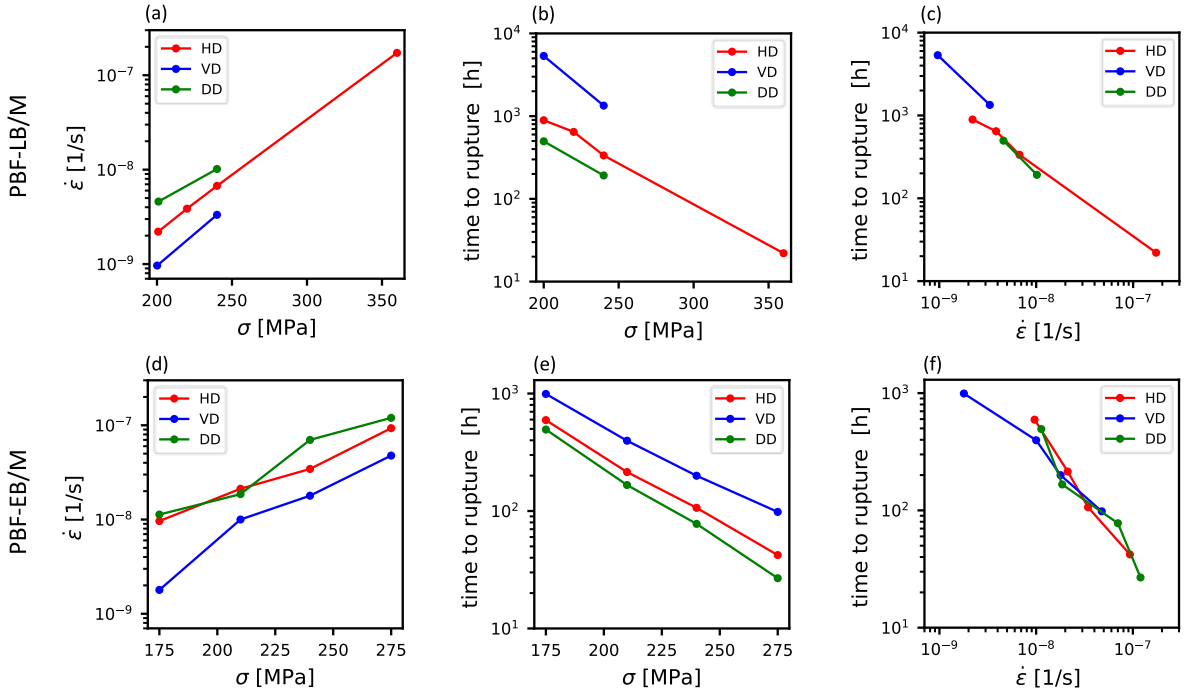

Fig. 5. Experimental creep test results at 850 °C for our PBF-LB/M specimens (top) and the PBF-EB/M specimens from [33] (bottom).

observed within the grains. The observed γ/γ' structure is similar to the conventionally manufactured IN738LC [82,83] with a bimodal γ' precipitate distribution composed of submicron-sized cuboidal primary γ' precipitates and nano-sized spherical secondary γ' precipitates, surrounded by the γ matrix, Fig. 4d. A volume fraction of 39% and a mean size of 0.38 μm were measured for the primary γ' precipitates. The periodicity length is estimated to be about 0.8 μm. The measured values are similar to the values given in the literature for the γ' volume fraction (40% to 43%), γ' precipitate mean size (0.5 to 0.7 μm), and the periodicity length (0.7 to 0.8 μm) reported in the literature for conventionally manufactured IN738LC [82–84]. Since no SEM-analysis results could be found for the PBF-EB/M material, we assumed the same values for the γ' volume fraction and the periodicity length as for our own PBF-LB/M material.

Compared to the current microstructure, the PBF-EB/M manufactured material [33] exhibits a sharper {001}-fiber texture in BD, a mean minor grain diameter of 50-100 μm, and a grain aspect ratio higher than 6. Figures S3-d to S3-f show the pole figures of the ODF functions reconstructed from [33] for the VD, DD, and HD specimens together with the loading direction.

3.2. Creep performance

The results of our creep experiments are plotted in Figs. 5a–c. Additionally, we reevaluated the creep data for PBF-EB/M specimens [33, 51] for comparison, Figs. 5d–f. All creep tests are performed at 850 °C. Figs. 5c and 5f present the correlation between rupture times and minimum strain rates, which in first approximation satisfy the Monkman–Grant (MG) relationship [85]: $\dot{\varepsilon}_{min}^{m} t_{rupt} = k$, where $\dot{\varepsilon}_{min}$ is the minimum creep rate, t_{rupt} the time to rupture and (m, k) orientation independent parameters.

The results in Fig. 5 show that despite the significant differences in texture and grain morphology, a clear and qualitatively similar anisotropy in the minimum creep rates and rupture times can be observed in both sets of materials. We also found that the creep rates (rupture times) for the DD and HD cases are rather similar, while these are significantly smaller (larger) for the VD case. These findings are in line with previous observations [48,86] reporting an anisotropic creep behavior (760 to 980 °C) of heat-treated AMed IN738LC, where a lower creep resistance was observed for their HD specimens compared to VD specimens. Such anisotropic creep behaviors highlight the significance of the complex AMed microstructure and the need for a deformation mechanistically-informed modeling to predict its anisotropic creep response. In practice, the successful application of AMed Ni-base superalloys in typical multi-axial stress conditions, such as in turbine blades, greatly requires prior, quantitative knowledge of creep anisotropy. To this end, we combined TEM analysis with modeling to investigate potential deformation mechanisms in a physically-sound manner. In addition to the results presented in Fig. 5, a comparison of creep performance was made between AMed and conventionally casted

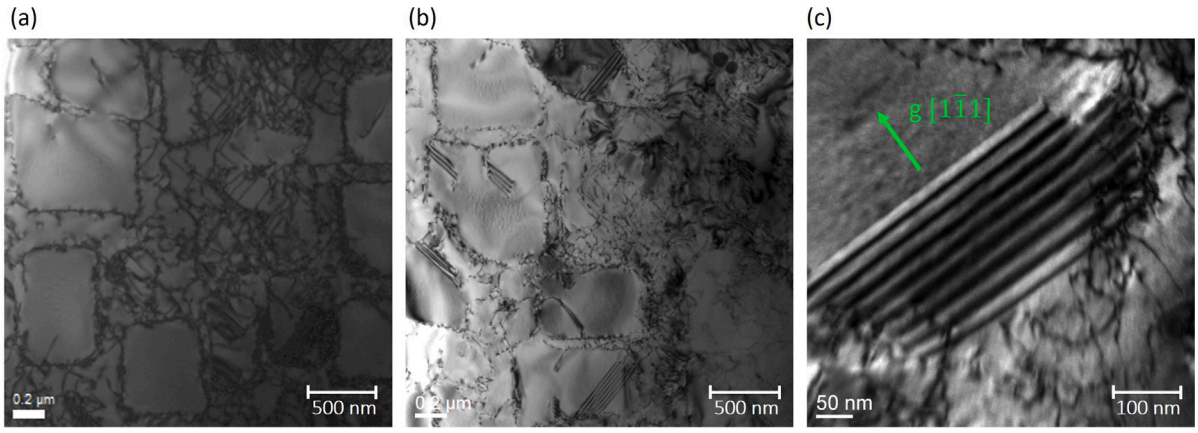

Fig. 6. Two-beam TEM analysis: (a) BF example of dislocation network at phase boundary interface recorded close to zone axis [001], (b) BF example of observed stacking faults with **g** =[020] recorded close to zone axis [001] and (c) example of detected SESF with annotated **g**-vector [1$\bar{1}$1] recorded close to the [$\bar{1}$12] zone axis are shown.

Table 3
Model parameters calibrated to the experiments. The equiaxed Voxel RVE (Fig. 2b) was used. Note that in the case of the octahedral systems in the matrix, $\tau_{\chi,c}$ is equal to τ_{Orwan}, which is calculated based on Eq. (15) and is not used as a fit parameter.

Material	Slip system χ		Octahedral		SISF	SESF
			Matrix	Precipitate		
PBF-LB/M	A_χ		1.67×10^{-7} [1/s]	4.07×10^{-12} [m/s]	1.60×10^{-8} [1/s]	1.24×10^{-8} [1/s]
	V_χ	[b^3]	101.8	22.8	259	195
	$\tau_{\chi,c}$	[MPa]	$\tau_{Orowan} = 104$	71	90	107
PBF-EB/M	A_χ		1.1×10^{-5} [1/s]	6.34×10^{-12} [m/s]	3.43×10^{-7} [1/s]	2.63×10^{-7} [1/s]
	V_χ	[b^3]	24.0	4.27	185	178
	$\tau_{\chi,c}$	[MPa]	$\tau_{Orowan} = 104$	22	152	124

(CC) IN738LC. The results are summarized in Fig. S6 in SM. The creep strength and creep rates of CC IN738LC are largely comparable to those of the PBF-LB/M materials in HD.

3.3. TEM evidence of active deformation mechanisms

In order to identify the deformation mechanisms, we performed TEM investigations that considered deformed samples in HD. Both dislocations in the γ phase and multiple stacking faults in the γ' phase were detected through two-beam conditions (Figs. 6a–b). We determined the character of the stacking faults following the methodology in [87]: By placing the origin of the **g**-vector at the center of the fault in a dark-field micrograph, it points towards the bright outer fringe, if it is intrinsic, or away from the bright outer fringe if it is extrinsic for 200, 222, and 440 reflections. The reverse correlation is true for 111, 220, and 400 reflections. The result is shown in Fig. 6c with a **g**-vector pointing away from the SF center, proving its extrinsic nature. Based on these results, we conclude that the SESF-related deformation mechanism, including microtwinning, should be active in AMed IN738LC at 850 °C. This is also in line with recent observations on microtwins in AMed IN738LC under creep deformation at 850 °C [49].

3.4. Modeling: the influence of slip systems and crystallographic texture on creep anisotropy

The results of TEM investigations suggest that the SESF-related slip systems from the type $\{111\} < \bar{2}11 >$ contribute to overall creep deformation and must be considered in CP modeling. Therefore, we used the natural capability of our modeling in which each of the three slip system families (SISF-related, SESF-related, OCT) can be activated or de-activated on purpose, which in turn gives different orientation dependencies of the creep rates for a single crystal. For example, the highest strain rate is achieved with SISF-related slip systems in [001] oriented crystals under tension, but for the SESF-related systems in [001] oriented crystals under compression [38,41].

To investigate the effect of the deformation mechanism choice on the creep anisotropy, we performed three series of simulations with equiaxed Voxel RVEs (Figs. 2e–f). Only one of the three slip system families χ is activated in each series. The respective material model parameters (A_χ, V_χ, $\tau_{\chi,c}$) were fitted to the HD creep results and are summarized in Table 3. The parameters that were not fitted are presented in Table S2 of the SM. The creep responses in the VD and DD directions were then calculated to validate the prediction of creep behavior. The simulation results and comparisons to the experimental data are shown in Fig. 7.

For our PBF-LB/M manufactured materials, a relatively small creep anisotropy is predicted. In particular, with the SESF-related systems, the predicted responses of all three orientations, VD, HD, and DD, appear to be very similar. Both SISF-related and octahedral slip systems yield a more pronounced anisotropic creep response but of opposite order.

In contrast, for the PBF-EB/M manufactured materials, a clear anisotropy is obtained for each of the three slip system families, Figs. 7d–f. This is expected due to the high intensity of the underlying texture.

The current results suggest that the crystallographic texture and the slip systems cannot solely be responsible for the experimentally observed creep anisotropy. We also conclude that the SESF-related systems are likely to play a more significant role than other deformation mechanisms, which is supported by our TEM investigations. Of course, it cannot be excluded that other deformation mechanisms are at least partially active. We want to emphasize that the parameters of the full model with all potentially active slip system families cannot be unambiguously determined without test data for the single crystal alloy in which the different slip system families are selectively activated. Therefore, we assume in the following that SISF-related and octahedral systems are not active. This assumption also helps us to expand our modeling's complexity, accounting for more precise microstructure features.

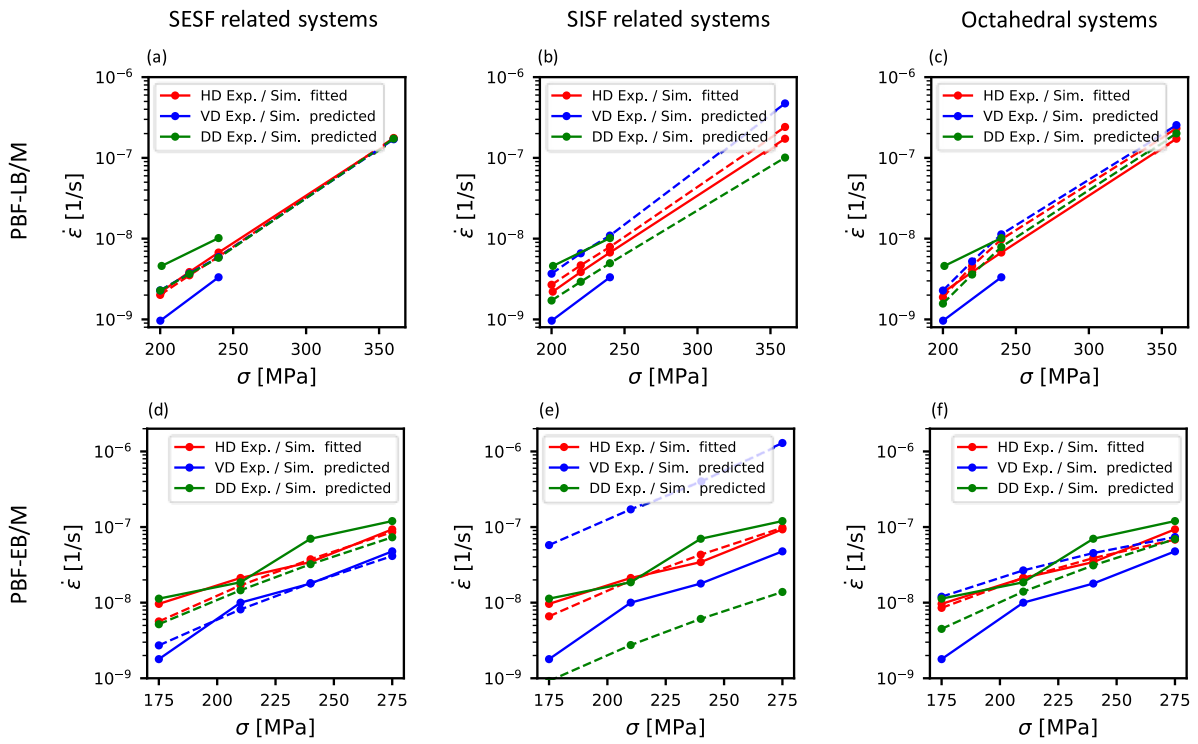

Fig. 7. Comparison of experimental (solid lines) and simulated (dashed lines) minimum creep rates for three slip systems and three specimen orientations. Creep experiments in HD are used to fit the data. Results in DD and VD are used for validation: (a) PBF-LB/M data set and SESF-related slip systems, (b) PBF-LB/M data set and SISF-related slip systems, (c) PBF-LB/M data set and octahedral slip systems, (d) PBF-EB/M data set and SESF-related slip systems, (e) PBF-EB/M data set and SISF-related slip systems and (f) PBF-EB/M data set and octahedral slip systems are shown.

3.5. Modeling: The influence of grain morphology on the creep anisotropy

In the next step, we considered Voxel and Voronoi RVEs (see Figs. 2e and 2i), with elongated grains to investigate the influence of grain morphology. For the PBF-LB/M material, aspect ratios of 3.0 and 2.85 were used, respectively, obtained from EBSD investigations (Fig. 3). All simulations in this section were performed with the parameters for the SESF-related systems provided in the last column of Table 3. Figs. 8a–c present the results, showing that grain morphology does not significantly affect the predicted creep rate for the VD and HD orientations. Interestingly, for the DD specimens, higher creep rates are predicted with elongated grains, which also yield better agreements with our creep data. The simulation results on the PBF-EB/M manufactured material (Figs. 8d–f) also confirm this behavior. In this case, a larger grain aspect ratio of 6.0 (Fig. 2f and Fig. 2j) was considered. The current results suggest that the grain morphology can influence the creep behavior depending on the loading conditions. In contrast, the choice of the Voxel or Voronoi model has only a limited impact on the creep rates.

3.6. Modeling: Combined effects of texture, grain morphology and deformation mechanisms

The effects of crystallographic texture, deformation mechanisms, and grain morphology can co-influence the creep behavior. Since the grain shape affects the creep rates, we refitted the parameters of the SESF-related slip systems to the data of the HD specimens using Voronoi RVEs with elongated grains (see Figs. 2h and 2j). The new parameters are summarized in Table 4.

Figs. 9a-b now show the comparison of minimum creep rates in consideration of all three combined effects. A clear improvement in the prediction of the creep rates in the VD and DD directions of the PBF-LB/M material can be observed. For a finer evaluation of the capabilities and limitations of the approach, we plotted the entire creep curves with a linear scale in Figs. 10a–f. Furthermore, a direct comparison of individual creep curves for each data set and stress level can be found in Figs. S4 and S5 of the SM. Note that both primary and secondary creep regimes are generally adequately represented, although the CP model does not explicitly include hardening effects. Indeed, the grains with a low creep rate constrain creep flow in the neighboring grains with a higher creep rate. This structural hardening can also be observed in all simulated curves. In all cases, the trends are reasonably predicted despite some deviations, mostly due to the amount of primary creep or an early start of creep acceleration. Specifically, the creep acceleration observed in several tests can explain the deviations between creep curves despite a relatively good agreement in measured and simulated minimum creep rates. Indeed, damage or softening mechanisms, as discussed for example in [88,89], are not included in the current model. However, we would like to stress that the present work's main objective is to identify the main factors responsible for creep anisotropy. An extension of the current approach is required for detailed and more accurate modeling of the whole creep response.

Table 4
Model parameters calibrated to the experiments, considering only SESF-related slip systems.

Data Set		PBF-EB/M	PBF-LB/M
A_{SESF}	[1/s]	5.30×10^{-8}	1.43×10^{-8}
V_{SESF}	[b^3]	208	199
$\tau_{SESF,c}$	[MPa]	168	114

4. Discussion

Despite their distinct crystallographic texture, the PBF-LB/M and PBF-EB/M specimens exhibit similar anisotropic creep responses, with a significant orientation dependence concerning the secondary and

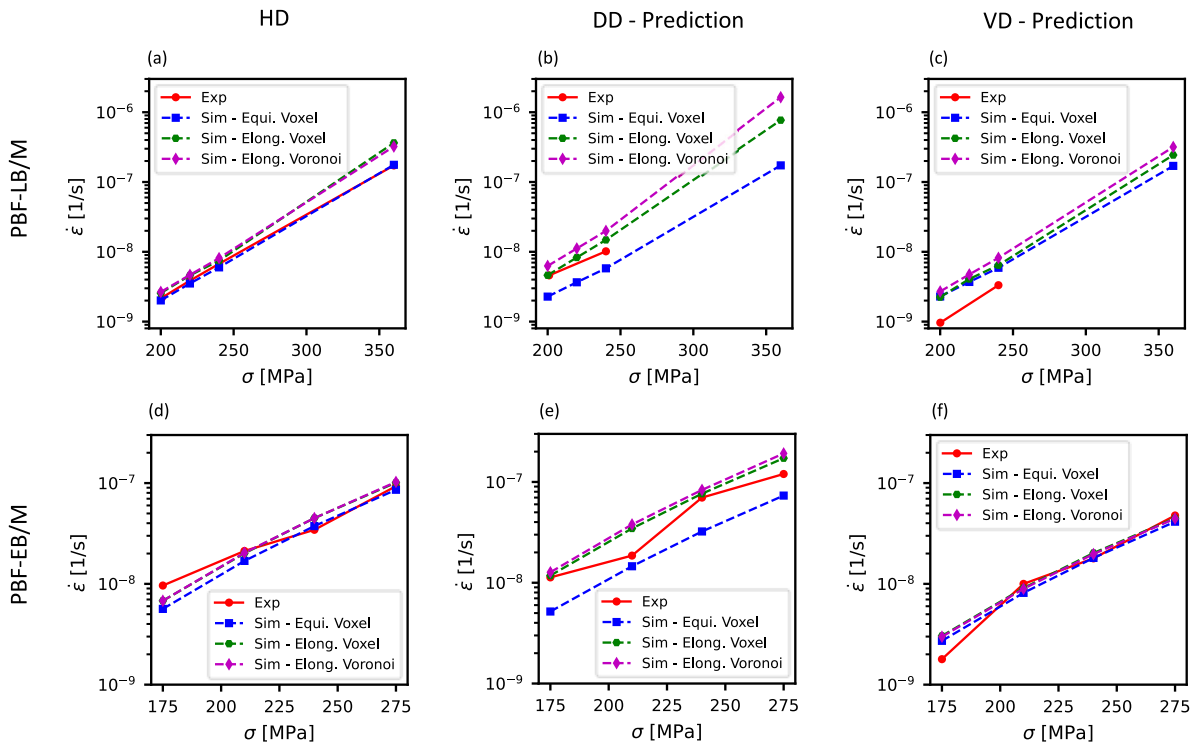

Fig. 8. Comparison of simulated creep responses for different grain morphologies (RVEs) and the SESF-related slip systems: (1) Equiaxed Voxel model, (2) Elongated Voxel model and (3) Elongated Voronoi model for PBF-LB/M data set (top) and PBF-EB/M data set (bottom).

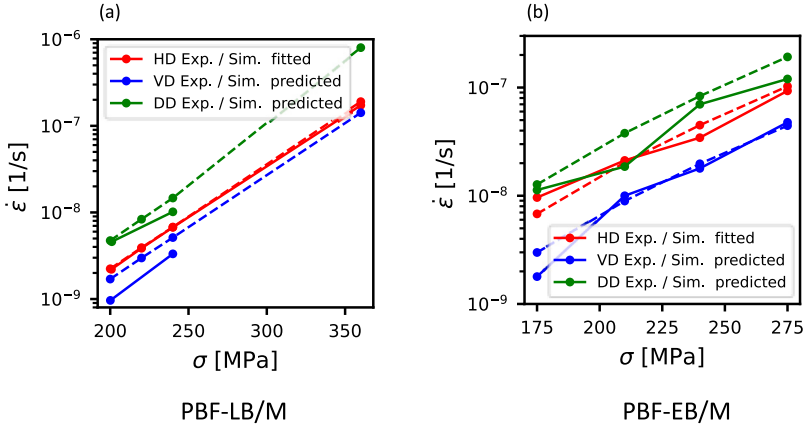

Fig. 9. Comparison of experimental (solid lines) and simulated (dashed lines) minimum creep rates with elongated Voronoi RVEs for PBF-LB/M data set (a) and PBF-EB/M data set from [33] (b).

tertiary regimes. The creep strength (minimum creep rate and rupture strain) is minimal in the DD and maximal in the VD specimens. The simulation results demonstrate that the crystallographic texture alone is insufficient to explain the observed stationary creep anisotropy. This is particularly interesting in our PBF-LB/M samples with a quite low texture index of 1.4. Hence, the necessity to consider additional microstructural factors, such as grain morphology, to explain the observed creep anisotropy becomes evident.

4.1. On the dominant deformation mechanisms

The results in Section 3.4 reveal that the predicted creep anisotropy strongly depends on the dominant deformation mechanisms and their corresponding slip systems. From the comparison of the creep response with different slip systems (Fig. 7), the SESF-related deformation mechanisms, i.e., isolated SESFs and/or microtwinning, are found to be the dominant deformation mechanisms. This finding is consistent with the relationship between the creep response and the crystallographic directions in a single crystal (SC) oriented along the highest orientation densities of AMed material, as discussed in the following.

To identify these orientations, the measured IPFs of the loading (z) direction for the HD, DD, and VD specimens are shown in Fig. 11. In the case of HD specimens, most grains are oriented in [001] or [011] directions. For the DD specimens, most grains are oriented in [011] direction, while for the VD specimens, most grains are oriented in [001] direction. Fig. 12 shows the predicted creep rates of SCs in the three tensile loading directions [001], [011] and [111], for each family of slip systems, and based on respective material parameter sets indicated in Table 3. The results indicate that the octahedral systems and the SISF-related systems exhibit the highest creep rates in the [001] direction, which, according to the IPFs presented in Fig. 11 would yield the highest creep rates for AMed specimens in VD, which is not the case in

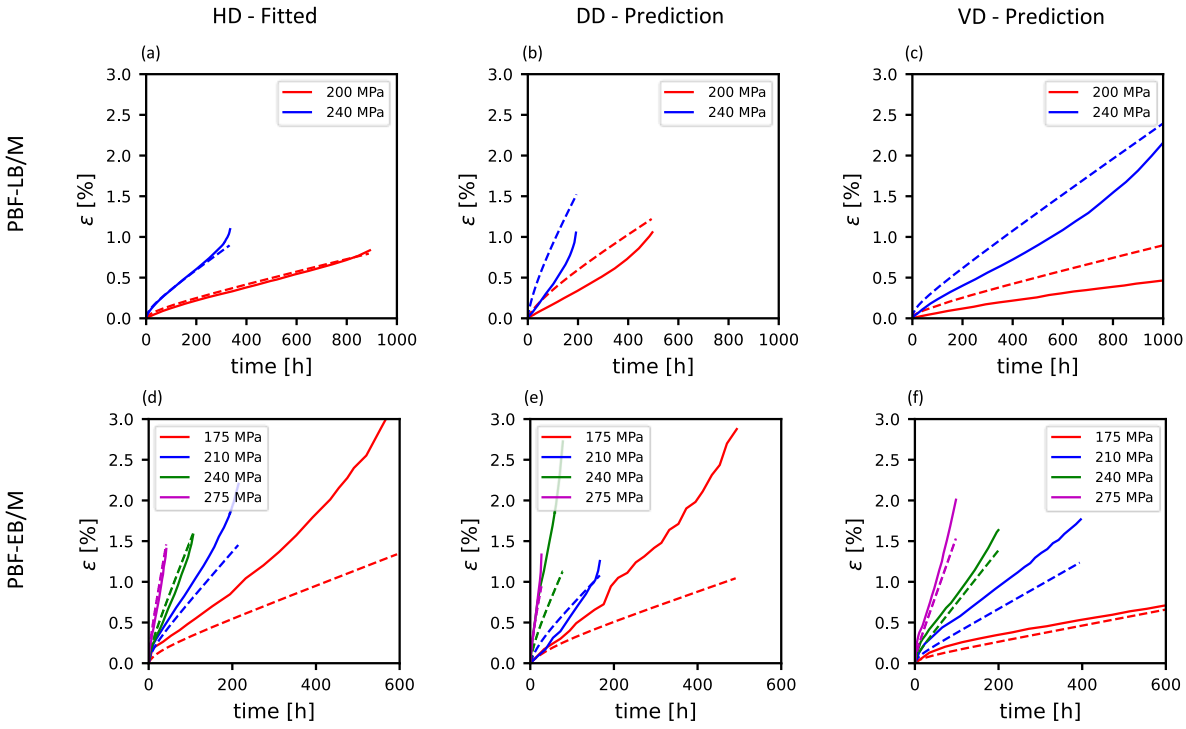

Fig. 10. Comparison of experimental (solid lines) and simulated (dashed) minimum creep curves with elongated Voronoi RVEs for PBF-LB/M data set (a–c) and PBF-EB/M data set from [33] (d–f).

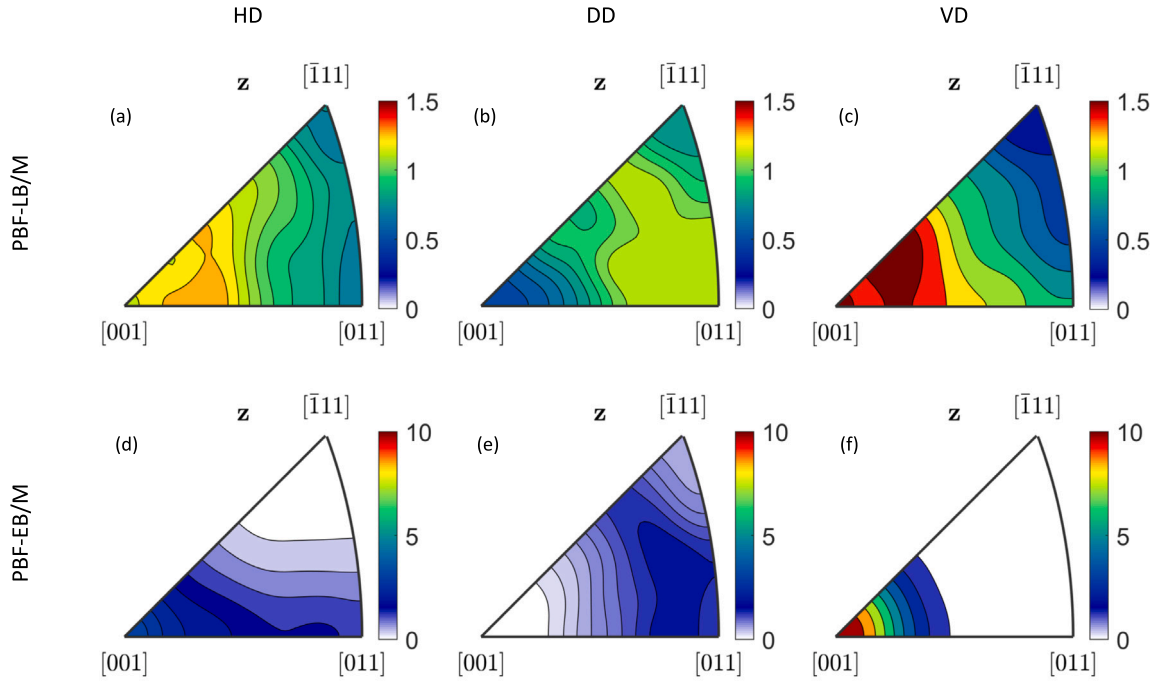

Fig. 11. IPFs of the loading direction (z) for HD, DD, and VD of PBF-LB/M (top) and PBF-EB/M (bottom) specimens.

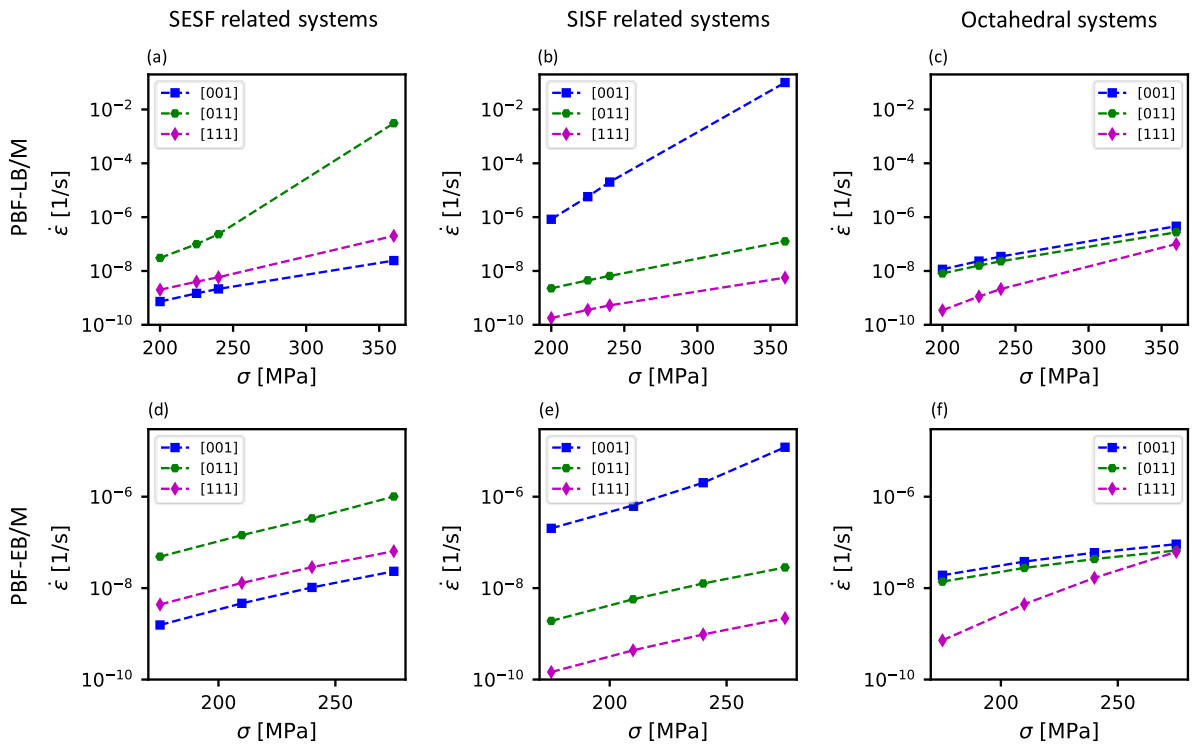

Fig. 12. Minimum creep rates for three SC specimen orientations and the six parameter sets of Table 3. The results for (a) PBF-LB/M and SESF-related slip systems, (b) PBF-LB/M and SISF-related slip systems, (c) PBF-LB/M and octahedral slip systems, (d) PBF-EB/M and SESF-related slip systems, (e) PBF-EB/M and SISF-related slip systems and (f) PBF-EB/M and octahedral slip systems are shown.

the experiments. Conversely, the SESF-related systems have the lowest (highest) creep rate in the [001] ([011]) direction, which would lead to the lowest (highest) predicted creep rates in the VD (DD) specimens. These results are in good agreement with the experimental measurements, thus confirming the dominance of the SESF-related deformation systems.

The results of the TEM investigations (Section 3.3) also confirm that SESFs are present in crept PBF-LB/M specimens, supporting the operation of SESF-related deformation mechanisms in the considered loading and temperature range. Furthermore, recent evidence via SEM analysis of the presence of microtwins in the same material and various specimen orientations was reported in [49]. Our findings are also in line with the current understanding of the formation of microtwins in Ni-base superalloys under creep, according to which SESFs can be regarded as the first stage of microtwins [26,39,41,60].

Despite the clear evidence for active SESFs-related deformation mechanisms revealed here, one should note that other deformation mechanisms can still be active before or together with the SESFs. In fact, it is well known that the deposition of matrix dislocations in the γ/γ' interfaces precedes the formation of the SESFs in the γ' precipitates (see, e.g., [26,39,60]). An exceptional characteristic of the AMed Ni-base superalloys is the massive chemical inhomogeneities throughout the microstructure. These may lead to varying stacking fault energies, which, in turn, affect the active deformation mechanisms. In the presence of such chemical inhomogeneities, chemo-mechanical coupling phenomena may also come into the picture [90–92]. Detailed information on the role of chemical inhomogeneity is scarce [93], requiring further microstructural analysis and calculations to quantify the share of the different deformation mechanisms. In this context, CP models coupled with mesoscale modeling of microstructural evolution and atomistic simulations on the chemo-mechanical coupling of linear and planar defects can dramatically enhance the ability of computational methods to predict the microstructure of AMed materials and their primary and secondary creep responses.

4.2. On the influence of grain morphology

The comparisons of the RVE simulation results with and without elongated grains show that the grain aspect ratio influences the predicted creep response, especially in the DD. Indeed, shearing is expected to be less constrained in the case of elongated grains with grain boundaries parallel to the maximal shear stress. This shows that RVE models with equiaxed grains are not acceptable for materials with a typical AMed microstructure. On the experimental side, several studies reported an influence of grain morphology on creep anisotropy in Ni-base polycrystalline superalloys. For example, revealing the dependency of the creep response on the grain size and aspect ratio in IN718 manufactured by the directed energy deposition technique [94], or demonstrating the combined influence of grain morphology and orientation in directionally solidified superalloys [95]. In addition to the considered deformation mechanisms in the present study, grain boundary sliding has been reported at intermediate and high-temperature ranges, as recently observed in PBF-LB/M manufactured IN738LC [96]. These results suggest that considering grain boundary sliding in RVE models could improve the capabilities of the modeling approach for predicting creep anisotropy.

5. Conclusions

We performed a coupled experimental investigation and microstructure-based modeling of the anisotropic creep response of PBF-LB/M manufactured IN738LC at 850 °C. To this aim, systematic studies on the influence of the active slip systems, the texture, and grain morphology were conducted on the microstructure and creep behavior of PBF-EB/M manufactured IN738LC. Based on our results:

- A clear anisotropy in secondary and tertiary creep response is observed with $\dot{\varepsilon}_{VD} < \dot{\varepsilon}_{HD} < \dot{\varepsilon}_{DD}$ for the minimum creep rate and $t_{VD} < t_{HD} < t_{DD}$ for the creep rupture time at a given stress level. The MG relationship can describe the correlation between the creep rate and the creep rupture time as a first approximation.

- An orientation dependence in the creep response persists, even after heat treatment, which is known to lower the texture intensity significantly. This demonstrates that the crystallographic texture alone is not sufficient to describe the measured creep anisotropy.
- Three relevant types of slip deformation mechanisms were studied, i.e., octahedral, SESF-related, and SISF-related. Activating each family of slip systems separately results in qualitatively different predictions of the creep anisotropy for the investigated microstructures. We found that considering the SESF-related slip systems as the dominant deformation mechanism is the only possible choice to describe the orientation dependency of the minimum creep rate.
- SESFs were observed in a TEM investigation of a crept specimen (PBF-LB/M condition), providing evidence for the activity of the SESF-related deformation mechanisms in the investigated loading range.
- The simulation results suggest that grain morphology and aspect ratio are partially responsible for the high creep rates observed in the DD specimens.

The current study underscores the value of integrating modeling with AM experiments to determine the processing-microstructure–property relationships. We demonstrated that our model can predict the processing-related anisotropy of the creep response of AMed IN738LC. In ongoing research, we are expanding the current modeling approach to encompass the effects of GB sliding and enhancing the CP model by coupling octahedral glide with SESF- and SISF-related mechanisms.

CRediT authorship contribution statement

K. Kianinejad: Writing – review & editing, Writing – original draft, Visualization, Validation, Software, Methodology, Formal analysis, Data curation, Conceptualization. **R. Darvishi Kamachali:** Writing – review & editing, Supervision, Investigation, Conceptualization. **A. Khedkar:** Software. **A.M. Manzoni:** Investigation. **L. Agudo Jácome:** Investigation. **S. Schriever:** Investigation. **R. Saliwan Neumann:** Investigation. **S. Megahed:** Investigation, Data curation. **C. Heinze:** Resources, Investigation. **S. Kamrani:** Investigation. **B. Fedelich:** Writing – review & editing, Writing – original draft, Supervision, Project administration, Methodology, Funding acquisition, Conceptualization.

Declaration of competing interest

The authors declare that they have no known competing financial interests or personal relationships that could have appeared to influence the work reported in this paper.

Data availability

Data will be made available on request.

Acknowledgments

The authors gratefully acknowledge the support from Werner von Siemens Centre for Industry and Science organization within the project high-temperature application (HTA 2.0) at BAM and co-founding via the European Regional Development Fund (ERDF).

Appendix A. Supplementary data

Supplementary material related to this article can be found online at https://doi.org/10.1016/j.msea.2024.146690. Supplementary materials associated with this work are attached.

References

[1] Abid Haleem, Mohd Javaid, Additive manufacturing applications in industry 4.0: A review, J. Ind. Integr. Manag. 04 (04) (2019) 1930001, http://dx.doi.org/10.1142/S2424862219300011.

[2] Maria Touri, Fatemeh Kabirian, Mahdi Saadati, Seeram Ramakrishna, Masoud Mozafari, Additive manufacturing of biomaterials - the evolution of rapid prototyping, Adv. Eng. Mater. 21 (2) (2019) 1800511, http://dx.doi.org/10.1002/adem.201800511, URL https://onlinelibrary.wiley.com/doi/abs/10.1002/adem.201800511.

[3] Abdollah Saboori, Alberta Aversa, Giulio Marchese, Sara Biamino, Mariangela Lombardi, Paolo Fino, Application of directed energy deposition-based additive manufacturing in repair, Appl. Sci. (ISSN: 2076-3417) 9 (16) (2019) http://dx.doi.org/10.3390/app9163316, URL https://www.mdpi.com/2076-3417/9/16/3316.

[4] K.R. Balasubramanian, V. Senthilkumar, Additive manufacturing of nickel-based super alloys for aero engine applications: SLM of inconel, in: A. Raja (Ed.), Additive Manufacturing Applications for Metals and Composites, IGI Global, 2020, http://dx.doi.org/10.4018/978-1-7998-4054-1.ch003.

[5] Dmytro Lesyk, Silvia Martinez, Vitaliy Dzhemelinkyi, Aitzol Lamikiz, Additive manufacturing of the superalloy turbine blades by selective laser melting: Surface quality, microstructure and porosity, in: Isak Karabegovic (Ed.), New Technologies, Development and Application III, Springer International Publishing, 2020, pp. 267–275.

[6] Olutayo Adegoke, Joel Andersson, Håkan Brodin, Robert Pederson, Review of laser powder bed fusion of Gamma-prime-strengthened nickel-based superalloys, Metals 10 (2020) 996.

[7] Bo Song, Xiao Zhao, Shuai Li, Changjun Han, Qingsong Wei, Shifeng Wen, Jie, Yusheng Shi, Differences in microstructure and properties between selective laser melting and traditional manufacturing for fabrication of metal parts: A review, Front. Mech. Eng. 10 (2) (2015) 111–125.

[8] Nana Kwabena Adomako, Nima Haghdadi, Sophie Primig, Electron and laser-based additive manufacturing of Ni-based superalloys: A review of heterogeneities in microstructure and mechanical properties, Mater. Des. (ISSN: 0264-1275) 223 (2022) 111245, http://dx.doi.org/10.1016/j.matdes.2022.111245, URL https://www.sciencedirect.com/science/article/pii/S026412752200867X.

[9] Yen-Ling Kuo, Shota Horikawa, Koji Kakehi, Effects of build direction and heat treatment on creep properties of Ni-base superalloy built up by additive manufacturing, Scr. Mater. (ISSN: 1359-6462) 129 (2017) 74–78, http://dx.doi.org/10.1016/j.scriptamat.2016.10.035, URL https://www.sciencedirect.com/science/article/pii/S1359646216305383.

[10] Salomé Sanchez, C.J. Hyde, I.A. Ashcroft, Ravi G.A., A.T. Clare, Multi-laser scan strategies for enhancing creep performance in LPBF, Addit. Manuf. (ISSN: 2214-8604) 41 (2021) 101948, http://dx.doi.org/10.1016/j.addma.2021.101948, URL https://www.sciencedirect.com/science/article/pii/S2214860421001135.

[11] Amir Mostafaei, Reza Ghiaasiaan, I-Ting Ho, Seth Strayer, Kai-Chun Chang, Nima Shamsaei, Shuai Shao, Santanu Paul, An-Chou Yeh, Sammy Tin, Albert C. To, Additive manufacturing of nickel-based superalloys: A state-of-the-art review on process-structure-defect-property relationship, Prog. Mater. Sci. (ISSN: 0079-6425) 136 (2023) 101108, http://dx.doi.org/10.1016/j.pmatsci.2023.101108, URL https://www.sciencedirect.com/science/article/pii/S0079642523000403.

[12] Chuan Guo, Gan Li, Sheng Li, Xiaogang Hu, Hongxing Lu, Xinggang Li, Zhen Xu, Yuhan Chen, Qingqing Li, Jian Lu, Qiang Zhu, Additive manufacturing of Ni-based superalloys: Residual stress, mechanisms of crack formation and strategies for crack inhibition, Nano Mater. Sci. (ISSN: 2589-9651) 5 (1) (2023) 53–77, http://dx.doi.org/10.1016/j.nanoms.2022.08.001, URL https://www.sciencedirect.com/science/article/pii/S2589965122000460.

[13] Suresh L. Chittewar, Nilesh G. Patil, Surface integrity of conventional and additively manufactured nickel superalloys: A review, Mater. Today: Proc. (ISSN: 2214-7853) 44 (2021) 701–708, http://dx.doi.org/10.1016/j.matpr.2020.10.614, URL https://www.sciencedirect.com/science/article/pii/S2214785320382377, International Conference on Materials, Processing and Characterization.

[14] Fabian Geiger, Karsten Kunze, Thomas Etter, Tailoring the texture of IN738LC processed by selective laser melting (SLM) by specific scanning strategies, Mater. Sci. Eng. A (ISSN: 0921-5093) 661 (2016) 240–246, http://dx.doi.org/10.1016/j.msea.2016.03.036, URL https://www.sciencedirect.com/science/article/pii/S0921509316302398.

[15] Fencheng Liu, Xin Lin, Chunping Huang, Menghua Song, Gaolin Yang, Jing Chen, Weidong Huang, The effect of laser scanning path on microstructures and mechanical properties of laser solid formed nickel-base superalloy inconel 718, J. Alloys Compd. (ISSN: 0925-8388) 509 (13) (2011) 4505–4509, http://dx.doi.org/10.1016/j.jallcom.2010.11.176, URL https://www.sciencedirect.com/science/article/pii/S0925838810029397.

[16] H. Helmer, A. Bauereiß, R.F. Singer, C. Körner, Grain structure evolution in inconel 718 during selective electron beam melting, Mater. Sci. Eng. A (ISSN: 0921-5093) 668 (2016) 180–187, http://dx.doi.org/10.1016/j.msea.2016.05.046, URL https://www.sciencedirect.com/science/article/pii/S0921509316305536.

[17] E. Hosseini, V.A. Popovich, A review of mechanical properties of additively manufactured inconel 718, Addit. Manuf. (ISSN: 2214-8604) 30 (2019) 100877, http://dx.doi.org/10.1016/j.addma.2019.100877, URL https://www.sciencedirect.com/science/article/pii/S221486041930226X.

[18] Shi-Hai Sun, Yuichiro Koizumi, Tsuyoshi Saito, Kenta Yamanaka, Yun-Ping Li, Yujie Cui, Akihiko Chiba, Electron beam additive manufacturing of inconel 718 alloy rods: Impact of build direction on microstructure and high-temperature tensile properties, Addit. Manuf. (ISSN: 2214-8604) 23 (2018) 457–470, http://dx.doi.org/10.1016/j.addma.2018.08.017, URL https://www.sciencedirect.com/science/article/pii/S2214860417303214.

[19] Arash P. Jirandehi, Behnam Hajshirmohammadi, Patricio Carrion, M.M. Khonsari, Nima Shamsaei, Shuai Shao, Strain energy-based fatigue failure analyses of LB-PBF inconel 718: Effect of build orientation, Addit. Manuf. (ISSN: 2214-8604) 52 (2022) 102661, http://dx.doi.org/10.1016/j.addma.2022.102661, URL https://www.sciencedirect.com/science/article/pii/S2214860422000677.

[20] Daijun Hu, Nicolò Grilli, Wentao Yan, Dislocation structures formation induced by thermal stress in additive manufacturing: Multiscale crystal plasticity modeling of dislocation transport, J. Mech. Phys. Solids (ISSN: 0022-5096) 173 (2023) 105235, http://dx.doi.org/10.1016/j.jmps.2023.105235, URL https://www.sciencedirect.com/science/article/pii/S002250962300039X.

[21] Yong Chen Yeoh, Guido Macchi, Ekta Jain, Bernard Gaskey, Sudharshan Raman, Grace Tay, Davide Verdi, Alin Patran, Antonio Mattia Grande, Matteo Seita, Multiscale microstructural heterogeneity and mechanical property scatter in inconel 718 produced by directed energy deposition, J. Alloys Compd. (ISSN: 0925-8388) 887 (2021) 161426, http://dx.doi.org/10.1016/j.jallcom.2021.161426, URL https://www.sciencedirect.com/science/article/pii/S0925838821028358.

[22] Patcharapit Promoppatum, Vitoon Uthaisangsuk, Part scale estimation of residual stress development in laser powder bed fusion additive manufacturing of inconel 718, Finite Elem. Anal. Des. (ISSN: 0168-874X) 189 (2021) 103528, http://dx.doi.org/10.1016/j.finel.2021.103528, URL https://www.sciencedirect.com/science/article/pii/S0168874X21000123.

[23] R. Reed, The superalloys. Fundamentals and applications., Cambridge University Press, 2006.

[24] G. Cailletaud, J. Cormier, G. Eggeler, V. Maurel, L. Nazé (Eds.), Nickel base single crystals across length scales, in: Nickel Base Single Crystals Across Length Scales, Elsevier, ISBN: 978-0-12-819357-0, 2022, pp. 341–469, http://dx.doi.org/10.1016/C2018-0-01723-5, URL https://www.sciencedirect.com/book/9780128193570/nickel-base-single-crystals-across-length-scales.

[25] T.M. Smith, R.R. Unocic, H. Deutchman, M.J. Mills, Creep deformation mechanism mapping in nickel base disk superalloys, Mater. High Temp. 33 (4–5) (2016) 372–383, http://dx.doi.org/10.1080/09603409.2016.1180858.

[26] D. Barba, E. Alabort, S. Pedrazzini, D.M. Collins, A.J. Wilkinson, P.A.J. Bagot, M.P. Moody, C. Atkinson, A. Jerusalem, R.C. Reed, On the microtwinning mechanism in a single crystal superalloy, Acta Mater. 135 (2017) 314–329, http://dx.doi.org/10.1016/j.actamat.2017.05.072.

[27] G. Cailletaud, S. Forest, D. Jeulin, F. Feyel, I. Galliet, V. Mounoury, S. Quilici, Some elements of microstructural mechanics, Comput. Mater. Sci. (ISSN: 0927-0256) 27 (3) (2003) 351–374, http://dx.doi.org/10.1016/S0927-0256(03)00041-7, URL https://www.sciencedirect.com/science/article/pii/S0927025603000417.

[28] G. Venkatramani, S. Ghosh, M. Mills, A size-dependent crystal plasticity finite-element model for creep and load shedding in polycrystalline titanium alloys, Acta Mater. (ISSN: 1359-6454) 55 (11) (2007) 3971–3986, http://dx.doi.org/10.1016/j.actamat.2007.03.017, URL https://www.sciencedirect.com/science/article/pii/S135964540700198X.

[29] F. Roters, P. Eisenlohr, L. Hantcherli, D.D. Tjahjanto, T.R. Bieler, D. Raabe, Overview of constitutive laws, kinematics, homogenization and multiscale methods in crystal plasticity finite-element modeling: Theory, experiments, applications, Acta Mater. (ISSN: 1359-6454) 58 (4) (2010) 1152–1211, http://dx.doi.org/10.1016/j.actamat.2009.10.058, URL https://www.sciencedirect.com/science/article/pii/S1359645409007617.

[30] Jiamei Zhang, Jianghua Li, Shengchuan Wu, Wenjie Zhang, Jingyu Sun, Guian Qian, High-cycle and very-high-cycle fatigue lifetime prediction of additively manufactured AlSi10Mg via crystal plasticity finite element method, Int. J. Fatigue (ISSN: 0142-1123) 155 (2022) 106577, http://dx.doi.org/10.1016/j.ijfatigue.2021.106577, URL https://www.sciencedirect.com/science/article/pii/S0142112321004278.

[31] Mahesh Prasad, Abhishek Biswas, Napat Vajragupta, Alexander Hartmaier, Identification of texture characteristics for improved creep behavior of a L-PBF fabricated IN738 alloy through micromechanical simulations, Modelling Simul. Mater. Sci. Eng. 30 (2022) http://dx.doi.org/10.1088/1361-651X/ac6e7a.

[32] Siwen Gao, Philip Wollgramm, Gunther Eggeler, Anxin Ma, Jürgen Schreuer, Alexander Hartmaier, A phenomenological creep model for nickel-base single crystal superalloys at intermediate temperatures, Modelling Simul. Mater. Sci. Eng. 26 (5) (2018) 055001, http://dx.doi.org/10.1088/1361-651X/aabdbe.

[33] Patxi Fernandez-Zelaia, Yousub Lee, Sebastian Dryepondt, Michael M. Kirka, Creep anisotropy modeling and uncertainty quantification of an additively manufactured Ni-based superalloy, Int. J. Plast. 151 (2022) 103177.

[34] S.S.K. Gunturi, D.W. MacLachlan, D.M. Knowles, Anisotropic creep in CMSX-4 in orientations distant from ⟨001⟩, Mater. Sci. Eng. A (ISSN: 0921-5093) 289 (1) (2000) 289–298, http://dx.doi.org/10.1016/S0921-5093(00)00829-7, URL https://www.sciencedirect.com/science/article/pii/S0921509300008297.

[35] D.M. Knowles, S. Gunturi, The role of ⟨112⟩{111} slip in the asymmetric nature of creep of single crystal superalloy CMSX-4, Mater. Sci. Eng. A (ISSN: 0921-5093) 328 (1) (2002) 223–237, http://dx.doi.org/10.1016/S0921-5093(01)01688-4, URL https://www.sciencedirect.com/science/article/pii/S0921509301016884.

[36] D.M. Knowles, Q.Z. Chen, Superlattice stacking fault formation and twinning during creep in γ/γ' single crystal superalloy CMSX-4, Mater. Sci. Eng. A (ISSN: 0921-5093) 340 (1) (2003) 88–102, http://dx.doi.org/10.1016/S0921-5093(02)00172-7, URL https://www.sciencedirect.com/science/article/pii/S0921509302001727.

[37] Duncan W. MacLachlan, Lawrence W. Wright, Satish Gunturi, David M. Knowles, Constitutive modelling of anisotropic creep deformation in single crystal blade alloys SRR99 and CMSX-4, Int. J. Plast. (ISSN: 0749-6419) 17 (4) (2001) 441–467, http://dx.doi.org/10.1016/S0749-6419(00)00058-9, URL https://www.sciencedirect.com/science/article/pii/S0749641900000589.

[38] C.M.F. Rae, R.C. Reed, Primary creep in single crystal superalloys: Origins, mechanisms and effects, Acta Mater. (ISSN: 1359-6454) 55 (3) (2007) 1067–1081, http://dx.doi.org/10.1016/j.actamat.2006.09.026, URL http://www.sciencedirect.com/science/article/pii/S1359645406006847.

[39] L. Kovarik, R.R. Unocic, Ju Li, P. Sarosi, C. Shen, Y. Wang, M.J. Mills, Microtwinning and other shearing mechanisms at intermediate temperatures in Ni-based superalloys, Prog. Mater. Sci. (ISSN: 0079-6425) 54 (6) (2009) 839–873, http://dx.doi.org/10.1016/j.pmatsci.2009.03.010, URL https://www.sciencedirect.com/science/article/pii/S0079642509000139.

[40] Bernard Fedelich, A microstructure based constitutive model for the mechanical behavior at high temperatures of nickel-base single crystal superalloys, Comput. Mater. Sci. (ISSN: 0927-0256) 16 (1) (1999) 248–258, http://dx.doi.org/10.1016/S0927-0256(99)00067-1, URL https://www.sciencedirect.com/science/article/pii/S0927025699000671.

[41] D. Barba, E. Alabort, D. Garcia-Gonzalez, J.J. Moverare, R.C. Reed, A. Jérusalem, A thermodynamically consistent constitutive model for diffusion-assisted plasticity in Ni-based superalloys, Int. J. Plast. (ISSN: 0749-6419) 105 (2018) 74–98, http://dx.doi.org/10.1016/j.ijplas.2017.12.007, URL https://www.sciencedirect.com/science/article/pii/S0749641917305624.

[42] A. Ma, D. Dye, R.C. Reed, A model for the creep deformation behaviour of single-crystal superalloy CMSX-4, Acta Mater. (ISSN: 1359-6454) 56 (8) (2008) 1657–1670, http://dx.doi.org/10.1016/j.actamat.2007.11.031, URL https://www.sciencedirect.com/science/article/pii/S135964540700804X.

[43] Yoon Suk Choi, Triplicane A. Parthasarathy, Christopher Woodward, Dennis M. Dimiduk, Michael D. Uchic, Constitutive model for anisotropic creep behaviors of single-crystal Ni-base superalloys in the low-temperature, high-stress regime, Metall. Mater. Trans. A (ISSN: 1543-1940) 43 (6) (2012) 1861–1869, http://dx.doi.org/10.1007/s11661-011-1047-7.

[44] M.Y. Nazmy, High temperature low cycle fatigue of IN 738 and application of strain range partitioning, Mater. Trans. A 14 (2) (1983) 449–461, http://dx.doi.org/10.1007/BF02644222.

[45] L. Rickenbacher, T. Etter, S. Hoevel, High temperature material properties of IN738LC processed by selective laser melting (SLM) technology, Proceeding of the ASTM 19 (2013) 282–290.

[46] B. Fedelich, A. Epishin, T. Link, H. Klingelhöffer, G. Künecke, P. Portella, Rafting during high temperature deformation in a single crystal superalloy: Experiments and modeling, Superalloys 2012 (2012) 491–500, http://dx.doi.org/10.1002/9781118516430.ch54,

[47] M.J. Anderson, A. Rowe, J. Wells, H.C. Basoalto, Application of a multi-component mean field model to the coarsening behaviour of a nickel-based superalloy, Acta Mater. (ISSN: 1359-6454) 114 (2016) 80–96, http://dx.doi.org/10.1016/j.actamat.2016.05.024, URL https://www.sciencedirect.com/science/article/pii/S1359645416303627.

[48] Jeroen Risse, Additive manufacturing of nickel-base superalloy IN738LC by laser powder bed fusion (Ph.D. thesis), RWTH Aacheb, 2019, pp. 190–195, http://dx.doi.org/10.18154/RWTH-2019-06822.

[49] Sandra Megahed, Karl Michael Krämer, Christoph Heinze, Christian Kontermann, Annett Udoh, Stefan Weihe, Matthias Oechsner, Influence of build orientation on the creep behavior of IN738LC manufactured with laser powder bed fusion, Mater. Sci. Eng. A (ISSN: 0921-5093) 878 (2023) 145197, http://dx.doi.org/10.1016/j.msea.2023.145197, URL https://www.sciencedirect.com/science/article/pii/S0921509323006214.

[50] DIN EN ISO 204:2019-04: Metallic materials - uniaxial creep testing in tension - method of test, 2019, p. 71, URL https://www.beuth.de/en/standard/din-en-iso-204/289976402.

[51] Patxi Fernandez-Zelaia, O.D. Acevedo, M.M. Kirka, D. Leonard, S. Yoder, Y. Lee, Creep behavior of high-gamma-prime Ni-based superalloy fabricated via electron beam melting, Metal. Master. Trans. 52 (2021) 574–590.

[52] F. Bachmann, Ralf Hielscher, Helmut Schaeben, Texture analysis with MTEX – free and open source software toolbox, in: Texture and Anisotropy of Polycrystals III, in: Solid State Phenomena, 160 (2010) 63–68, http://dx.doi.org/10.4028/www.scientific.net/SSP.160.63.

[53] John M. Sosa, Brain Welk, Daniel E. Huber, Hamish L. Fraser, Development and application of MIPAR: a novel software package for two- and three-dimensional microstructural characterization, Integr. Mater. Manuf. Innov. (2014) http://dx.doi.org/10.1186/2193-9772-3-10.

[54] Shahriyar Keshavarz, Somnath Ghosh, Multi-scale crystal plasticity finite element model approach to modeling nickel-based superalloys, Acta Mater. (ISSN: 1359-6454) 61 (17) (2013) 6549–6561, http://dx.doi.org/10.1016/j.actamat.2013.07.038, URL https://www.sciencedirect.com/science/article/pii/S1359645413005582.

[55] Masoud Ghorbani Moghaddam, Ajit Achuthan, Brett A. Bednarcyk, Steven M. Arnold, Evan J. Pineda, Grain size-dependent crystal plasticity constitutive model for polycrystal materials, Mater. Sci. Eng. A (ISSN: 0921-5093) 703 (2017) 521–532, http://dx.doi.org/10.1016/j.msea.2017.07.087, URL https://www.sciencedirect.com/science/article/pii/S0921509317309930.

[56] M. Pinz, G. Weber, W.C. Lenthe, M.D. Uchic, T.M. Pollock, S. Ghosh, Microstructure and property based statistically equivalent RVEs for intragranular gamma - gamma' microstructures of Ni-based superalloys, Acta Mater. (ISSN: 1359-6454) 157 (2018) 245–258, http://dx.doi.org/10.1016/j.actamat.2018.07.034, URL https://www.sciencedirect.com/science/article/pii/S1359645418305627.

[57] A. Charmi, R. Falkenberg, L. Ávila, G. Mohr, K. Sommer, A. Ulbricht, M. Sprengel, R. Saliwan Neumann, B. Skrotzki, A. Evans, Mechanical anisotropy of additively manufactured stainless steel 316L: An experimental and numerical study, Mater. Sci. Eng. A (ISSN: 0921-5093) 799 (2021) 140154, http://dx.doi.org/10.1016/j.msea.2020.140154, URL https://www.sciencedirect.com/science/article/pii/S092150932031220X.

[58] R.W. Kozar, A. Suzuki, W. Milligan, Strengthening mechanisms in polycrystalline multimodal nickel-base superalloys, Metall. Mater. Trans. A 40 (2009) 1543–1940, http://dx.doi.org/10.1007/s11661-009-9858-5.

[59] M. Kolbe, The high temperature decrease of the critical resolved shear stress in nickel-base superalloys, Mater. Sci. Eng. A (ISSN: 0921-5093) 319–321 (2001) 383–387, http://dx.doi.org/10.1016/S0921-5093(01)00944-3, URL https://www.sciencedirect.com/science/article/pii/S0921509301009443.

[60] F.D. León-Cázares, F. Monni, C.M.F. Rae, Stress orientation dependence for the propagation of stacking faults and superlattice stacking faults in nickel-based superalloys, Acta Mater. (ISSN: 1359-6454) 199 (2020) 209–224, http://dx.doi.org/10.1016/j.actamat.2020.08.032, URL https://www.sciencedirect.com/science/article/pii/S1359645420306297.

[61] X. Wu, A. Dlouhy, Y.M. Eggeler, E. Spiecker, A. Kostka, C. Somsen, G. Eggeler, On the nucleation of planar faults during low temperature and high stress creep of single crystal Ni-base superalloys, Acta Mater. (ISSN: 1359-6454) 144 (2018) 642–655, http://dx.doi.org/10.1016/j.actamat.2017.09.063, URL https://www.sciencedirect.com/science/article/pii/S1359645417308339.

[62] F.D. León-Cázares, R. Schlütter, F. Monni, M.C. Hardy, C.M.F. Rae, Nucleation of superlattice intrinsic stacking faults via cross-slip in nickel-based superalloys, Acta Mater. (ISSN: 1359-6454) 241 (2022) 118372, http://dx.doi.org/10.1016/j.actamat.2022.118372, URL https://www.sciencedirect.com/science/article/pii/S1359645422007509.

[63] R.V. Miner, T.P. Gabb, J. Gayda, K.J. Hemker, Orientation and temperature dependence of some mechanical properties of the single-crystal nickel-base superalloy René N4: Part iii. tension-compression anisotropy, Metallurgical Transactions A (ISSN: 1543-1940) 17 (3) (1986) 507–512, http://dx.doi.org/10.1007/BF02643957.

[64] D. Bettge, W. Österle, "Cube slip" in near-[111] oriented specimens of a single-crystal nickel-base superalloy, Scr. Mater. (ISSN: 1359-6462) 40 (4) (1999) 389–395, http://dx.doi.org/10.1016/S1359-6462(98)00446-1, URL https://www.sciencedirect.com/science/article/pii/S1359646298004461.

[65] A. Vattré, B. Devincre, A. Roos, Orientation dependence of plastic deformation in nickel-based single crystal superalloys: Discrete–continuous model simulations, Acta Mater. (ISSN: 1359-6454) 58 (6) (2010) 1938–1951, http://dx.doi.org/10.1016/j.actamat.2009.11.037, URL https://www.sciencedirect.com/science/article/pii/S1359645409008167.

[66] M. McLean, On the threshold stress for dislocation creep in particle strengthened alloys, Acta Metall. (ISSN: 0001-6160) 33 (4) (1985) 545–556, http://dx.doi.org/10.1016/0001-6160(85)90018-5, URL https://www.sciencedirect.com/science/article/pii/0001616085900185.

[67] D. Mukherji, R.P. Wahi, Some implications of the particle and climb geometry on the climb resistance in nickel-base superalloys, Acta Mater. (ISSN: 1359-6454) 44 (4) (1996) 1529–1539, http://dx.doi.org/10.1016/1359-6454(95)00274-X, URL https://www.sciencedirect.com/science/article/pii/135964549500274X.

[68] D. Dye, H.J. Stone, R.C. Reed, A two phase elastic–plastic self-consistent model for the accumulation of microstrains in waspaloy, Acta Mater. (ISSN: 1359-6454) 49 (7) (2001) 1271–1283, http://dx.doi.org/10.1016/S1359-6454(01)00003-9, URL https://www.sciencedirect.com/science/article/pii/S1359645401000039.

[69] B. Fedelich, On the cubic slip effect and anisotropy modeling of single crystal superalloys at intermediate temperature, 2023, In preparation.

[70] M.M. Mehrabadi, S.C. Cowin, Eigenvectors of linear anisotropic elastic materials, Quart. J. Mech. Appl. Math. 43 (1) (1990) 15–41, http://dx.doi.org/10.1093/qjmam/43.1.15.

[71] A.S. Krausz, H. Eyring, Deformation kinetics, John Wiley and Sons, New York, 1975.

[72] Bernard Fedelich, Georgia Künecke, Alexander Epishin, Thomas Link, Pedro Portella, Constitutive modelling of creep degradation due to rafting in single-crystalline Ni-base superalloys, Mater. Sci. Eng. A 510 (2009) 273–277, http://dx.doi.org/10.1016/j.msea.2008.04.089.

[73] T. Mura, Micromechanics of defects in solids, Kluwer, 1982.

[74] T.M. Smith, B.D. Esser, N. Antolin, G.B. Viswanathan, T. Hanlon, A. Wessman, D. Mourer, W. Windl, D.W. McComb, M.J. Mills, Segregation and eta phase formation along stacking faults during creep at intermediate temperatures in a Ni-based superalloy, Acta Mater. (ISSN: 1359-6454) 100 (2015) 19–31, http://dx.doi.org/10.1016/j.actamat.2015.08.053, URL https://www.sciencedirect.com/science/article/pii/S1359645415006308.

[75] Z-set software, 2017, URL http://zset-software.com.

[76] J.A. Nelder, R. Mead, A Simplex Method for Function Minimization, Comput. J. (ISSN: 0010-4620) 7 (4) (1965) 308–313, http://dx.doi.org/10.1093/comjnl/7.4.308.

[77] R. Quey, P.R. Dawson, F. Barbe, Large-scale 3D random polycrystals for the finite element method: Generation, meshing and remeshing, Comput. Methods Appl. Mech. Engrg. (ISSN: 0045-7825) 200 (17) (2011) 1729–1745, http://dx.doi.org/10.1016/j.cma.2011.01.002, URL https://www.sciencedirect.com/science/article/pii/S004578251100003X.

[78] Considering computational speed vs. accuracy: Choosing appropriate mesoscale RVE boundary conditions, Comput. Methods Appl. Mech. Engrg. (ISSN: 0045-7825) 374 (2021) 113572, http://dx.doi.org/10.1016/j.cma.2020.113572, URL https://www.sciencedirect.com/science/article/pii/S004578252030757X.

[79] Kenjiro Terada, Muneo Hori, Takashi Kyoya, Noboru Kikuchi, Simulation of the multi-scale convergence in computational homogenization approaches, Int. J. Solids Struct. (ISSN: 0020-7683) 37 (16) (2000) 2285–2311, http://dx.doi.org/10.1016/S0020-7683(98)00341-2, URL https://www.sciencedirect.com/science/article/pii/S0020768398003412.

[80] Ansys Academic Research Mechanical, URL https://www.ansys.com/.

[81] Karsten Kunze, Thomas Etter, Jürgen Grässlin, Valery Shklover, Texture, anisotropy in microstructure and mechanical properties of IN738LC alloy processed by selective laser melting (SLM), Mater. Sci. Eng. A (ISSN: 0921-5093) 620 (2015) 213–222, http://dx.doi.org/10.1016/j.msea.2014.10.003, URL https://www.sciencedirect.com/science/article/pii/S0921509314012362.

[82] D. Bettge, W. Oesterle, J. Ziebs, Temperature dependence of yield strength and elongation of the nickel-base IN-738 and nichrome, Zeitschrift fuer Metalkunde 85 (1995).

[83] Ercan Balikci, R.A Mirshams, A. Raman, Influence of various heat treatments on the microstructure of polycrystalline IN738LC, Metall. Mater. Trans. A 28 (1997) http://dx.doi.org/10.1007/s11661-997-0156-9.

[84] J. Li, R.P. Wahi, Investigation of gamma-gamma' lattice mismatch in the polycrystalline nickel-base superalloy IN738LC: Influence of heat treatment and creep deformation, Acta Metall. Mater. (ISSN: 0956-7151) 43 (2) (1995) 507–517, http://dx.doi.org/10.1016/0956-7151(94)00252-D, URL https://www.sciencedirect.com/science/article/pii/095671519400252D.

[85] F.C. Monkman, N.J. Grant, Deformation and fracture at elevated temperatures, third ed., Proceeding of the ASTM 56 (1956) 593–597.

[86] H.Y. Song, M.C. Lam, Y. Chen, S. Wu, P.D. Hodgson, X.H. Wu, Y.M. Zhu, A.J. Huang, Towards creep property improvement of selective laser melted Ni-based superalloy IN738LC, J. Mater. Sci. Technol. (ISSN: 1005-0302) 112 (2022) 301–314, http://dx.doi.org/10.1016/j.jmst.2021.09.050, URL https://www.sciencedirect.com/science/article/pii/S1005030221010124.

[87] J.W. Edington, Interpretation of transmission electron micrographs, 1975, http://dx.doi.org/10.1007/978-1-349-02658-6.

[88] P.J. Henderson, M. McLean, Microstructural contributions to friction stress and recovery kinetics during creep of the nickel-base superalloy IN738LC, Acta Metall. (ISSN: 0001-6160) 31 (8) (1983) 1203–1219, http://dx.doi.org/10.1016/0001-6160(83)90182-7, URL https://www.sciencedirect.com/science/article/pii/0001616083901827.

[89] James Coakley, David Dye, Hector Basoalto, Creep and creep modelling of a multimodal nickel-base superalloy, Acta Mater. (ISSN: 1359-6454) 59 (3) (2011) 854–863, http://dx.doi.org/10.1016/j.actamat.2010.08.035, URL https://www.sciencedirect.com/science/article/pii/S1359645410005495.

[90] Francis Larché, John W. Cahn, A linear theory of thermochemical equilibrium of solids under stress, Acta Metall. 21 (8) (1973) 1051–1063.

[91] R. Darvishi Kamachali, E. Borukhovich, O. Shchyglo, I. Steinbach, Solutal gradients in strained equilibrium, Phil. Mag. Lett. 93 (12) (2013) 680–687.

[92] Reza Darvishi Kamachali, Christian Schwarze, Inverse ripening and rearrangement of precipitates under chemomechanical coupling, Comput. Mater. Sci. 130 (2017) 292–296.

[93] H. Hasan, P. Mlkvik, P.D. Haynes, V.A. Vorontsov, Generalised stacking fault energy of Ni-Al and Co-Al-W superalloys: Density-functional theory calculations, Materialia 9 (2020) 100555.

[94] Ying Li, Jaromír Dlouhý, Jaroslav Vavřík, Jan Džugan, Pavel Konopík, Tomáš Krajňák, Jozef Veselý, Investigation of short-term creep properties of a coarse-grained inconel 718 fabricated by directed energy deposition compared to traditional inconel 718, Mater. Sci. Eng. A (ISSN: 0921-5093) 844 (2022) 143143, http://dx.doi.org/10.1016/j.msea.2022.143143, URL https://www.sciencedirect.com/science/article/pii/S0921509322005482.

[95] B. DeMestral, G. Eggeler, H.-J. Klam, On the influence of grain morphology on creep deformation and damage mechanisms in directionally solidified and oxide dispersion strengthened superalloys, Metall. Mater. Trans. A (ISSN: 1543-1940) 27 (4) (1996) 879–890, http://dx.doi.org/10.1007/BF02649755.

[96] Jinghao Xu, Hans Gruber, Dunyong Deng, Ru Lin Peng, Johan J. Moverare, Short-term creep behavior of an additive manufactured non-weldable nickel-base superalloy evaluated by slow strain rate testing, Acta Mater. (ISSN: 1359-6454) 179 (2019) 142–157, http://dx.doi.org/10.1016/j.actamat.2019.08.034, URL https://www.sciencedirect.com/science/article/pii/S1359645419305464.